A novel, RAS-independent role for *NF1* in microtubular dynamics and damage repair dictates sensitivity to T-DM1 in HER2-positive breast cancer

Bruno A. Duso[1*], Eleonora Messuti[1*], Giulia Tini[1], Emanuele Bonetti[1], Alessia Castiglioni[1], Gianmaria Frigè[1], Giuseppe Ciossani[1], Silvia Monzani[1], Chiara Soriani[1], Daria Khuntsariya[2], Nicolò Roda[1], Andrea Polazzi[1], Marica R. Ippolito[1], Elena G. Doronzoro[1], Eltjona Mane[3], Alessia Farfalla[4], Costantino Jemos[4], Elena Guerini-Rocco[3], Simona Rodighiero[1], Daniela Tosoni[1], Stefano Santaguida[1], Marcus Braun[2], Zdeněk Lánský[2], Luigi Scietti[1], Pier Giuseppe Pelicci[1] and Luca Mazzarella[1#]

.Affiliations:
1. Dept of Experimental Oncology, IRCCS European Institute of Oncology, Milan Italy
2. Institute of biotechnology, CAS, BIOCEV, Prague West Czech Republic
3. Division of Pathology, IRCCS European Institute of Oncology, Milan Italy
4. Clinical Pharmacy, IRCCS European Institute of Oncology, Milan Italy

*these authors contributed equally

correspondence to:
Dr Luca Mazzarella
Dept of Experimental Oncology,
IRCCS European Institute of Oncology,
Via Adamello 16, Milan 20143
Italy
Luca.mazzarella@ieo.it

Running title. NF1 controls microtubule dynamics

Keywords; Neurofibromatosis, microtubules, antibody-drug conjugate, breast cancer, HER2

Word count (excluding methods): 3921
Figures: 6
Tables: 0
Supplementary figures: 4
Supplementary tables: 3
Supplementary movies: 12

Abstract

The gene neurofibromatosis 1 (NF1) is increasingly recognized as a key somatic driver of cancerogenesis, in addition to its well-known role as the germline determinant of the onco-developmental syndrome Neurofibromatosis. NF1 is best characterized as a negative regulator of RAS activation, but several lines of evidence suggest that it may have additional, poorly characterized functions.

In breast cancer, NF1 loss is known to be associated with resistance to endocrine and HER2-targeted therapy. Here, using HER2+ breast cancer cell lines engineered to ablate NF1 by CRISPR-Cas9 and in vitro reductionist models, we show that NF1 is a bona fide Microtubule-Associated Protein (MAP) with a novel, RAS-independent role in regulating dynamic instability and intra-lattice repair of microtubules. We show that loss of NF1 results in multiple mitotic defects (enlarged mitotic plate, delayed mitotic exit, supranumerary centrosomes and chromosome misalignment) that generate a low-grade aneuploidy that can also be measured as increased aneuploidy score in breast cancer patients bearing pathogenic NF1 mutations. Loss of NF1 leads to increased sensitivity to the approved Antibody-Drug Conjugate T-DM1 and in particular to its payload of the maytansin family, thus representing the first payload-specific predictive biomarker.

These findings highlight a novel function for an established tumor suppressor and support the assessment of NF1 status to guide tailored treatment decision in breast cancer

Introduction

Neurofibromatosis 1 (*NF1*) was one of the first tumor suppressor genes identified [1]. Loss of function mutations in *NF1* are at the basis of the onco-developmental syndrome neurofibromatosis and are frequently observed at the somatic level across multiple tumors [2]. In breast cancer, *NF1* loss of function has been implicated in resistance to both endocrine and anti-HER2 agents [3–5]. This has been attributed to the best characterized activity of NF1, its GTPase-activating protein (GAP) function that attenuates RAS signalling[6]. In the absence of NF1, RAS becomes constitutively activated, phenocopying signaling aberrations like growth factor-independence characteristic of canonical RAS mutations[6–8]. *NF1* encodes Neurofibromin (NF1), a large multifunctional protein consisting of 2,818 amino acids [9]. Because of its large size and difficulty in cloning, NF1 structure has resisted structural characterization for several years, and only recently high-resolution reconstructions by Cryo-EM have been obtained [10,11]. Still, despite the identification of several NF1 interactors, the vast majority of biochemical studies have focused only on its interaction with RAS, as the RAS-interacting domain (GRD) can be easily cloned and purified. Early studies provided evidence for an interaction with tubulin, which could be co-purified with NF1 in insect cells [7]; shortly thereafter, NF1 was found to co-localize with microtubules in immunofluorescence [12]. Two regions in NF1 have been proposed to mediate its interaction with tubulin: a "tubulin-binding domain" (TBD) localized to the 80 residues N-terminal of the GRD, and the C-Terminal Domain (CTD) [13]. The physiological relevance of this interaction remains uncertain, and NF1 is not generally included among *bona fide* Microtubule-Associated Protein (MAP) [14].

Our understanding of microtubular dynamics has been significantly modified in recent years by the finding that dynamic changes do not only occur at the microtubule end but also within the lattice, where the mechanical stress induced by motors or other sources generates discontinuities that are continuously repaired by intra-lattice tubulin incorporation [15,16]. To date, only two MAPs, CLASP and SSNA1 [17,18] have been found to recognize and modulate intratubular damage, but it is likely that other cellular factors are involved in this process.

Microtubules are a key target for anti-cancer therapy. In recent years, numerous powerful microtubule-depolymerizing agents have been exploited as payloads for Antibody-Drug Conjugates (ADC) [19], which have revolutionized the therapeutic landscape in oncology, leading to unprecedented survival advantages across multiple cancer types [20]. In some tumors like breast cancer (BC), multiple ADCs have been approved and several more are in development, generating an increasing demand for biomarkers predictive of response to inform clinical decisions. Although all three components of ADCs (antibody, linker and payload) may be differently impacted by tumor/host biomarkers, research has so far focused mostly on antibody targets. However, there is increasing recognition that ADC activity is not simply determined by the levels of expression of their cognate antigen [20]. No clear payload-associated predictive biomarker has been identified to date. In HER2+ breast cancer (BC), an area in which ADC development has been particularly disruptive, there are now two approved agents (Trastuzumab Emtansine, T-Dxd, and Trastuzumab Deruxtecan, T-Dxd) and several in development, all targeting the same receptor (HER2), in some cases with the same antibody (Trastuzumab), but differing by linker and payload [21]. Thus, rational treatment choices between ADCs is likely to be dictated by tumor-intrinsic differences in payload sensitivity.

Among payloads, derivatives of maytansine like DM1 have played a critical role and remain actively researched drugs. Maytansine was identified from the plant Maytenus Ovatus in the 70s but initially failed in clinical trials due to its low therapeutic index [22]. Its use in the context of ADCs in the 2000s allowed to significantly reduce toxicity while attaining significant efficacy and led to the first ADC approval in breast cancer [23]. Uniquely among microtubule-targeting agents, the maytansine binding site becomes inaccessible once tubulin is incorporated in the microtubule lattice, as it is positioned at the interface between two tubulin dimers [24]. Thus, maytansine is currently thought to act by inhibiting de novo tubulin incorporation at the microtubule end, a model consistent with experiments showing decreased dynamicity in purified microtubules [25]. However, precise measurement of binding stoichiometry revealed a number of binding sites for S-methyl-DM1 in excess to the theoretical 13 exposed sites at each microtubule [25]. A further conundrum in maytansine pharmacology is the vastly higher active concentration between in vitro (in the micromolar range) vs in cells (in the nanomolar range), suggesting that the cellular context includes factors able to enhance maytansine activity [26].

Here, we investigate the role of NF1 in HER2+ BC. We show that NF1 loss is a common event in metastatic HER2+ BC and is associated with resistance to some agents but increased sensitivity specifically to T-DM1 but not T-Dxd. This sensitization is due to a RAS-independent activity of NF1 on the modulation of microtubular dynamicity and damage.

Results

1. *NF1* is differentially mutated in metastatic *vs* primary HER2+ BC and its loss leads to differential sensitivity to several agents

In an effort to identify genes potentially involved in resistance to conventional anti-HER2 agents in breast cancer, we compared the frequency of mutation occurrence between metastatic and primary HER2-amplified breast cancer, since virtually all metachronous metastases in HER2+ BC develop after exposure to targeted agents, typically at least Trastuzumab. We pooled publicly available datasets of BC sequencing (TCGA and MSK-IMPACT/GENIE[27,28]) and identified primitive (n=1487) *vs* metastatic (n=813) cases. We compared frequencies of mutated genes in the overall cohort and in the *ERBB2*-amplified subgroup, identified based on copy number data rather than histological HER2 status, which is often unreported or unreliable. *NF1* was identified as the most significant differentially mutated gene between metastatic and primary HER2+ BC (OR=5.14, pvalue=2.93 x 10^{-4}, adj pvalue=0.01, figure 1A); in the overall cohort, *NF1* was also more frequently mutated in metastatic than in primary, but this was comparatively less significant (OR=1.739, pvalue=0.00249, adj pvalue=1, supplementary figure 1A). The mutational spectrum in metastatic tumors was indicative of loss of function and typical of a tumour-suppressor gene, dominated by nonsense and missense mutations scattered throughout the gene (figure 1B-C).
To investigate the biological consequences of *NF1* loss in HER2+ BC, we generated *NF1* KO clones of the widely used HER2+ BC cell line BT-474, SKBR3 and HCC1954 using CRISPR/Cas9 technology (supplementary figure 1B). We then subjected BT-474^{WT} and BT-474^{KO} cells to a pharmacological screen with all drugs currently approved for treatment, including chemotherapeutics, monoclonal antibodies, Tyrosine-Kinase Inhibitors (TKI) and antibody-drug conjugates. We decided to use a 3-day BrdU incorporation assay, which we found to have a wider dynamic range for short-term assays with slow-proliferating cells like BT-474. For many agents, in particular pertuzumab, IC_{50} values were higher, supporting the idea that *NF1* loss is associated resistance to standard HER2-targeting agents and in agreement with results of a recent study in which NF1 levels were lowered by RNA interference [4] (figure 1D). Unexpectedly, BT-474^{KO} exhibited a ~ 5 fold reduction in IC50 for T-DM1. This differential sensitivity became more apparent in longer term growth curves (figure 1E) and in coculture experiments in which BT-474^{WT} and BT-474^{KO} cells were differentially labelled with mCherry and GFP respectively (figure 1F). Differential sensitivity was confirmed in SK-BR3 and HCC1954 cells (supplementary figure 1C).

2. NF1 loss leads to increased G2/M arrest and apoptosis upon T-DM1 treatment both in vitro and in vivo

In BT-474^{KO} cells, T-DM1 led to enhanced G2/M arrest compared to BT-474^{WT} cells (figure 2A-B), which could be observed by simple visual inspection of growing cells (figure 2C-D), and induction of apoptosis markers (cleaved PARP and reduced Bcl2, figure 2E). Furthermore, residual cells after T-DM1 treatment stained more strongly with the senescence marker beta-galactosidase in BT-474^{KO} vs BT-474^{WT} cells (supplementary figure 2A).
To further characterize cell cycle dynamics, we engineered BT-474^{WT} and BT-474^{KO} to express the FUCCI(Ca) reporter [29], which allows the monitoring of G1, S and G2M phases in live cell imaging experiments in which the addition of the DRAQ7 live cell dye also allowed to identify dying cells. The kinetics of cell death was similar in BT-474^{WT} and BT-474^{KO} cells, initiating ~ 30 hrs after T-DM1 administration (figure 2F-G), with death typically occurring upon exit from M phase or right after re-entry in G1 (supplementary figure 2B). T-DM1-treated BT-474^{KO} cell exhibited significantly prolonged G2/M phase and higher death rates compared to BT-474^{WT} cells (figure 2F-I).
Then, we tested if the differential activity could also be observed in vivo. We chose the HCC-1954 model as it provides faster, more reliable and estrogen-independent *in vitro* growth kinetics compared to BT-474 and SK-BR3. We injected luciferase-expressing HCC-1954^{WT} and HCC-1954^{KO} cells in the two opposite flanks of Nod-Scid-IL2GR Ko (NSG) mice, which we randomized to treatment with either vehicle or T-DM1 at days 15

and 29. Vehicle-treated tumors did not exhibit differential growth between HCC-1954^{WT} and HCC-1954^{KO} masses, whereas T-DM1 resulted in significantly stronger growth inhibition of HCC-1954^{KO} vs HCC-1954^{WT} tumors (figure 2K-L). Histological analysis of tumors retrieved 24 hours after T-DM1 treated revealed a significantly higher apoptotic index and cleaved Caspase 3 in HCC-1954^{KO} masses (figure 2M-N).
We conclude that genetic ablation of NF1 leads to increased sensitivity to T-DM1 both *in vitro* and *in vivo*

3. NF1 loss-associated hypersensitivity to T-DM1 is due to the DM1 payload and is RAS-independent

We then elucidated if differential response to T-DM1 is due to biological factors affecting antibody binding/internalization or response to the DM1 payload. BT-474^{KO} did not exhibit higher levels of HER2 expression (supplementary figure 3A). Immunofluorescence for endocytosed T-DM1 did not reveal any major difference in ADC internalization (supplementary figure 3B-C). Conversely, treatment of cells with the cell-permeable naked payload DM1 was more effective in BT-474^{KO} compared to BT-474^{WT} cells in long-term growth curves (figure 3A) and colony-formation assays (figure 3B-D), similarly to T-DM1 and differently from Trastuzumab alone, which showed reduced inhibitory activity in BT-474^{KO} cells. Also, no difference could be observed between WT and KO cells in the response to the other ADC approved in HER2+ BC, T-Dxd, by colony formation (figure 3E). DM1 was also the only differentially sensitive microtubule-targeting agent, among the many tested (vinblastine, paclitaxel, MMAE, Paclitaxel, Pironetin, supplementary figure 3C).
We then investigated if hypersensitivity to T-DM1 is reproduced by oncogenic RAS signalling activation, which is often phenocopied by NF1 loss. We generated BT-474 cells expressing pathogenic p.G12V KRAS (BT-474 ^{G12V}). These cells exhibited the expected RAS hyperactivation per RAS-GTP pulldown assays (figure 3F), similar or higher than that achieved by NF1 loss. We did not observe any major difference in long-term growth neither in unperturbed conditions nor upon treatment with T-DM1 or DM1 (figure 3G). Additionally, RAS-GTP pulldown assays in NF1-KO cells showed heterogeneous effects on RAS activation state, which was only moderately increased in SK-BR3^{KO} cells, (supplementary figure 3D) despite similar effect on T-DM1 sensitivity.
Thus, we conclude that increased sensitivity to T-DM1 upon NF1 loss is due specifically to the DM1 payload and is not a consequence of RAS hyperactivation

4. NF1loss leads to mitotic aberrations and aneuploidy

To further characterize the global changes induced by *NF1* loss and T-DM1 treatment, we analysed the transcriptome of BT-474^{KO} and BT-474^{WT} cells subjected to T-DM1 treatment. Principal component analysis (PCA) of RNAseq performed showed clear segregation of biological replicates with genotype and treatment (figure 4A). When we compared transcriptional changes induced by T-DM1, we identified a set of 256 genes downregulated more strongly in BT-474^{KO} compared to BT-474^{WT} cells (figure 4B and supplementary table 1). Gene Ontology analysis revealed that these genes were enriched for terms related to mitosis and mitotic spindle (figure 4C and supplementary table 2). These findings further suggested a role for NF1 in modulating microtubules and mitosis, so we investigated in detail this hypothesis.
We monitored mitosis duration and anomalies using live cell imaging of cells engineered to express H2B-GFP to follow mitotic chromatin condensation and SiR-tubulin to monitor spindle formation. KO cells exhibited significantly prolonged mitosis and evidence for lagging chromosomes and pseudodipolar mitoses (figure 4D and supplementary video 1-3). KO cells showed an enlarged mitotic plate (figure 4E). Immunofluorescence for tubulin and centrosome markers CEP63 in HCC1954 cells synchronized by either the CDK1 inhibitor RO3306 or double thymidine block confirmed that HCC1954^{KO} cells are characterized by a significantly higher prevalence of cells with supranumerary centrosomes (figure 4F), which lead to pseudo-dipolar mitoses that require prolonged spindle adjustments and may at least partially explain the delayed exit from M phase observed in live cell imaging. Altered mitosis is associated with the acquisition of chromosomal aberrations, so we measured the impact of NF1 loss on aneuploidy. In synchronized cells, HCC1954^{KO} cells exhibited an increased rate of chromosome misalignment (figure 4G) and a higher fraction of cells exhibiting >2n DNA content in cell culture as measured by flow cytometric cell cycle analysis (figure 4H). To verify if NF1 loss is a clinically relevant determinant of tumor aneuploidy, we computed the aneuploidy score (AS) [30] from cancer sequencing data of breast cancer patients in the AACR GENIE cohort

[31]. As shown in figure 4I, patients with an NF1 mutation predicted to have a pathogenic impact according to Alpha Missense [32] showed a moderately but significantly higher AS compared to those without.
Thus, we conclude that NF1 loss leads to important mitotic aberrations that favour the acquisition of a moderate degree of aneuploidy.

5. NF1 is a microtubule-associated protein (MAP)

We then investigated the nature of the NF1-microtubule interaction. We performed immunofluorescence (IF) with antibodies against tubulin and NF1. We used the only commercially available antibody clone that showed adequate signal specificity after extensive testing against KO cells with multiple protocols (supplementary figure 4A) [5]. Immunofluorescence (IF) showed that NF1 has a diffuse microgranular pattern and increases in intensity in mitotic cells, with a pattern that overlaps with the mitotic spindle in anaphase (figure 5A). To study the biochemistry of NF1 interaction with tubulin and microtubules, we purified NF1 from insect cells, using an NF1 expression vector[33] that we modified by introducing a PreScission cleavage site (HRV 3C site) to eliminate the His tag after purification, as previous studies showed that its positively charged residues may generate spurious interactions with microtubules[34]. Full-length NF1 exhibited the expected biochemical properties as it could be purified with high purity and efficiency by size-exclusion chromatography (SEC) (supplementary figures 4B-C), it allowed efficient His-tag removal (supplementary figures 4D), could be eluted as a predominant 623 kDa entity, compatible with the known dimeric form of NF1 (supplementary figure 4E) and exhibited GTPase-Activating Protein (GAP) activity on RAS (supplementary figure 4F).
To test whether NF1 directly binds to microtubules, we performed a classical microtubule co-sedimentation assay. Purified NF1 was fully soluble, but incubation with tubulin subjected to polymerization cycles led to NF1 co-sedimentation with microtubules in the insoluble pellet (figure 5B). In conventional turbidity-based tubulin polymerization assays, purified NF1 led to a significant acceleration of the polymerization curve, with a loss of the initial nucleation phase (figure 5C). NF1 decreased the critical tubulin concentration, ie the minimal concentration to initiate polymerization (supplementary figure 4G). Microscopic inspection of MT formed in the presence of NF1 revealed the formation of microtubule bundles (figure 5D), a property shared by several MAPs [14], which may also contribute to turbidity increase and complicate the interpretation of bulk polymerization assays. To remove the effect of bundle formation, we assessed the dynamics of individual microtubules by Total Internal Reflection Fluorescence (TIRF) microscopy on microtubules forming on glass-immobilized seeds. The addition of NF1 led to a dose-dependent increase in the fraction of microtubules initiating elongation (figure 5E), elongation speed (figure 5F) and catastrophe frequencies (figure 5G) and rescue frequency (figure 5H and supplementary movies 1-3).

6. DM1 leads to intratubular damage that is repaired more efficiently in the presence of NF1

To characterize how NF1 loss modulates the pharmacodynamics of DM1 in cells, we performed Cellular Thermal Shift Assay (CETSA). DM1 led to a right shift in the tubulin melting curve, indicative of tubulin stabilization and target engagement; comparison of BT-474^{WT} vs BT-474^{KO} cells showed a significant right shift of the melting curve in BT-474^{KO} cells, indicating that DM1 engages tubulin more efficiently in BT-474^{KO} cells than in BT-474^{WT} (figure 6A-C).
We then applied TIRF to microtubules treated with DM1, with or without NF1. DM1 led, as expected [25], to a reduction in the fraction of elongating microtubules and in elongation speed. Addition of recombinant NF1 dose-dependently inhibited DM1 activity and allowed microtubular polymerization, to the point that at 300 nM NF1 the fraction of polymerizing microtubules was completely rescued (figure 6D-F and supplementary videos 4-6). In conditions favoring depolymerization (low free tubulin concentration) of taxol-stabilized microtubules, DM1 accelerated depolymerization rate as expected. Addition of NF1 significantly reduced depolymerization rate both in control and treated microtubules (figure 6G). Additionally, we observed the appearance of several areas of intra-lattice reduction in tubulin density upon DM1 treatment , suggestive of tubulin eviction from the lattice. In areas where tubulin density approached zero, we observed the occurrence of microtubule fracturing (figure 6H). These findings suggests that DM1 is able to bind to intra-lattice sites, in addition to its known ability to bind dimeric tubulin or microtubule tips[26] and cause or

amplify intratubular damage. In the presence of NF1, DM1-induced intratubular damage sites were filled by de novo tubulin incorporation (figure 6I).

Finally, to study microtubular dynamics in response to NF1 loss and DM1 treatment in a cellular environment, we engineered BT-474^{KO} and BT-474^{WT} cells to express the EB3-GFP reporter, which binds to microtubular tips and allows their tracking by live cell imaging [35]. Upon reconstruction of tip trajectories, we calculated in vivo dynamics parameters. In the absence of treatment, average microtubule growth speed was not significantly different between BT-474^{KO} and BT-474^{WT} cells, but upon DM1 treatment, the number of elongating microtubules and microtubule speed were significantly reduced in BT-474^{KO} cells (figure 6J-K), paralleling the findings from TIRF microscopy. Finally, to support the idea that NF1 loss leads to in vivo accumulation of intra-lattice microtubular damage, we stained HCC1954^{WT} and HCC1954^{KO} cells (as the HCC1954 cells allow a better visualization of the microtubular network than other cell types) with antibodies against K40-acetylated alpha tubulin, which has been proposed to accumulate in microtubule bodies due to the entry of the acetyltransferase aTAT1 through intra-lattice discontinuities [36]. We found that HCC1954^{KO} had a significantly higher level of K40-acetylated alpha tubulin compared to HCC1954^{WT} cells (figure 6K-L).

We conclude that NF1 enhances microtubular dynamics and favors the repair of intra-lattice damage, which represents a novel and pharmacologically relevant site of action for maytansinoids.

Discussion

In this work we provide evidence for a previously underappreciated role for NF1 in regulating microtubular dynamics and lattice integrity. We show that this activity is crucial to preserve genomic stability and is a liability targetable by approved antibody-drug conjugates in HER2+ BC.

The interaction between microtubules and NF1 was identified early on in the 90s, shortly after NF1 cloning [12,37,38], but its physiological significance has remained poorly characterized to date. Colocalization studies have been contradictory. The earliest study [12] did not observe colocalization with mitotic spindle microtubules on NIH3T3, mouse and kangaroo fibroblasts, whereas a recent study [13] on glioblastoma cell lines identified an NF1 isoform able to bind the spindle and essential for proper chromosome segregation. Both these studies were conducted with currently unavailable antibodies, and came to different conclusions regarding the NF1 domain responsible for the interaction with microtubules.

In our study we demonstrate that NF1 is a bona fide MAP, as it co-sediments with microtubules in vitro, induces microtubule bundling, decreases the critical concentration for tubulin polymerization and enhances microtubule dynamic instability.

In breast cancer cells, NF1 loss appears crucial for a normal mitosis, since its loss leads to increased mitotic plate size, delayed mitosis exit, accumulation of supranumerary centrosomes and chromosome missegregation. These mitotic defects collectively favor chromosomal instability (CIN) that leads to low-grade aneuploidy, identifiable both in cell culture and in patients. It is likely that NF1-induced CIN contributes to both decreased sensitivity to antiblastic agents and the metastatic phenotype [39,40], explaining the frequent occurrence of NF1 as a sub-clonal, late-appearing genetic alteration during tumor evolution [41].

Importantly, NF1 effect on microtubule dynamics and mitosis appears independent from its activity on RAS. The expression of a constitutively active, oncogenic RAS mutant does not reproduce the sensitization to DM1 induced by NF1 ablation; furthermore, NF1 enhancement of microtubule dynamics occurs in vitro in the absence of any additional protein, and can therefore be defined an intrinsic property of NF1.

Two regions residing in distant areas of the NF1 protein (a C-terminal domain and a tubulin-binding domain next to the RAS-interacting domain) have been proposed to mediate interaction with tubulin [12,13], but structural data are currently missing. A testable and fascinating hypothesis is that MT dynamics is enhanced by NF1 by promoting the intrinsic GTP-hydrolizing activity of beta-tubulin, which favors the stabilization of the tubulin newly incorporated in the lattice. This model would recall the established GTPase-activating protein (GAP) function of NF1 on RAS; it must be stressed that early experiments did not identify a GAP activity using tubulin as a substrate; tubulin was, however, able to decrease NF1 GAP activity on RAS, suggesting that the two GTPAses may be competing for the same active site on NF1. The structural and

functional domains responsible for the MT-NF1 interaction remain to be characterized and are the subject of ongoing research.

We show that DM1 treatment induces intra-lattice breaks, which appear to be repaired more efficiently in the presence of NF1. The concept that MT lattice bears physiological discontinuities that are continuously repaired in vivo is relatively new [15], and may inform a better understanding of the mechanism of action of maytansinoids. The maytansin binding site, uniquely among MT-targeting agents, resides at the interface between two tubulin dimers [24]. In the current paradigm, maytansin is thought to be able to bind only dimeric tubulin and microtubule ends, leading to inhibition of de novo tubulin polymerization or microtubule depolymerization from the extremities. This model is supported by experiments specifically assessing either de novo tubulin polymerization or microtubule instability [25,26]. Our TIRF experiments using stabilized microtubules allowed to show that DM1 treatment leads not only to microtubule shortening but also to intra-lattice reduction in tubulin density, which in extreme cases lead to full microtubule breakage. We argue that this is allowed by the exposure of intra-lattice maytansin binding sites due to the lattice discontinuities that are now known to be generated upon taxol- or GMPCPP-induced MT stabilization in vitro [42]. NF1 joins the expanding ranks of proteins proposed to contribute to microtubular damage repair, which currently includes CLASP and SSNA1 [17,18]. To what degree this function contributes to the pathophysiological manifestations of NF1 loss, including neurodevelopmental defects observed in neurofibromatosis remains to be explored.

Our results further support the usefulness of NF1 status as a clinically meaningful biomarker for treatment choices in BC. NF1 status is able to predict sensitivity to endocrine therapy[3,5,43], targeted therapy (ref [4] and this study) and ADCs (this study). In particular, NF1 represents, to our knowledge, the first ADC payload-associated predictive biomarker to be identified, shedding light on the molecular mechanism underlying a major conundrum in ADC research: the reason for heterogeneous responses across patients with similar expression levels of the antibody target [20]. NF1 status can be assessed in the clinics by targeted NGS, albeit with reserves due to the significant presence of NF1 homologous sequences across the genome and the wide variety of mutations [2]. We believe the implementation of NF1 assessment in the routine diagnostics for breast and other cancers will contribute to the development of better tailored treatments for cancer patients

Acknowledgements

We would like to acknowledge drs Anna De Antoni, at IFOM Milan, Marina Mapelli, Stefano Freddi and Simona Ronzoni at IEO, Carsten Janke at Institut Curie, Fabrice Andre at Institut Gustave Roussy and Andrea Prota at the Paul Scherrer Institut for help with experimental design; Dominic Esposito for sharing the plasmid R702-X38-635 through Addgene

Funding

This project was funded by a My First AIRC grant to LM n 25791. BAD is the recipient of a FIEO fellowship 2023

Author contribution

Conceptualization: BAD, EM and LM. Methodology: GT, EB, AC, GF, GC, SM, CS, DK, NR, AP, MI, ED, EM, AF, CJ, EGR, SR, DT, SS, MB ZL, LS, PGP, LM. Verification: AC, EM, GT, EB. Formal Analysis: BAD, EM, GT, EB. Investigation: GT, EB, AC, GF, GC, SM, CS, DK, NR, AP, MI, ED, EM, AF, CJ, EGR, SR, DT. Writing: BAD, EM, GT, AC, EM, LM. Writing review: all authors

Competing Interests

All authors declare no conflict of interest

Materials & Methods

Cell lines and cell culture

BT-474, SK-BR-3, HCC1954 and MDA-MB-231 cells were purchased from American Type Culture Collection (ATCC). The two former were cultured in Dulbecco's modified Eagle's medium (DMEM, 12800-017; Gibco, Grand Island, NY, USA) while the latter in RPMI-1640 (GE healthcare, Memphis, TN, USA). Both were supplemented with 10% fetal bovine serum (FBS, 10099-141; Life Technologies, Carlsbad, CA, USA), 100 U/mL penicillin and 100 mg/mL streptomycin and kept in a humidified 5% CO_2 atmosphere at 37°C.

CRISPR-Cas9 generation of NF1KO clones

An sgNF1 (FWD: ACGGCCTGGACCCATTCCAC; REV: GTGGAATGGGTCCAGGCCGT) targeting exon 1 was selected based on best on-target/off-target scores provided by Benchling (https://benchling.com/), San Francisco, CA, USA. The guide was cloned into pSpCas9(BB) 2A-GFP (PX458) plasmid421, a gift from Feng Zhang (Addgene #48138). A DNA fragment containing 248nt of the NF1 coding region of interest was PCR-amplified from single-strand cDNA obtained from parental and clonal cells using QIAquick Gel Extraction Kit (QIAGEN). Incorporation was confirmed by Sanger sequencing the amplicon. All three cell lines were subsequently transfected with the plasmid containing the NF1 gRNA in parallel with empty vector controls using Lipofectamine 2000 according to manufacturer's instructions. Seventy-two hours later, GFP-positive cells were single-cell sorted in 96-well plates. For the ribonucleoprotein (RNP)-mediated knockout of NF1 performed on BT-474 cells, Gene Knockout Kit v2 was ordered from Synthego (https://www.synthego.com/) and the Cas9 protein was purified in the institute, as a gift of L Rizzuti (Department of Experimental Oncology, European Institute of Oncology, Milan). RNP were assembled and lipofected into cells following the manufacturer's instruction. After clonal expansion, knockout efficiency was analysed by western blot against neurofibromin and further characterised with NGS.

NGS-based validation of CRISPR knockout

Genomic DNA extraction was performed using the DNeasy Blood & Tissue Kit (Qiagen), in accordance with the manufacturer's instructions. DNA concentrations were carried out using Qubit dsDNA Broad Range quantification assay kit (Thermo Fisher Scientific). Libraries were generated using TruSight Rapid Capture kit in combination with the TruSight Cancer Sequencing Panel (Illumina) according to the manufacturer's protocol. Briefly, 50 ng of gDNA was enzymatically fragmented and adaptor sequences were added to the ends. The tagmented DNA was amplified by PCR followed by purification. Target regions were captured with Cancer Sequencing Panel probes followed by PCR amplification and purification of the enriched library. Quantification of enriched libraries was performed with Qubit dsDNA High Sensitivity quantification assay kit (Thermo Fisher Scientific) and library size distribution was measured with Bioanalyzer 2100 and High Sensitivity DNA Kit (Agilent Technologies). Final DNA libraries sequencing was performed in Illumina NovaSeq 6000 platform using the NovaSeq 6000 S1 Reagent Kit 300 cycles (2 x 150 paired-end reads) (Illumina). Sequencing data were analysed with Illumina DRAGEN Bio-IT Platform v4.0 using proprietary pipelines for variant calling. The resulting VCF with detected variants files were were annotated and classified with the GATK-Funcotator.

High-throughput drug screen

BT-474^{WT} and BT-474^{KO} cells were seeded (1 x 10^4) in 96-well, white-bottom plates (Corning), in triplicates, and incubated overnight. Then, specified compounds were added in 9 dilutions plus their respective vehicle. After 96h, BrdU reagent was incorporated for additional 24h followed by fixation and detection according to manufacturer's instructions (Cell Signalling Technology, #5492). Luminescence was read using a PHERAstar FSX Microplate Reader under a 425nm wavelength. The relative response was corrected compound-wise to the average vehicle response for each replicate. Data were analyzed in GraphPad Prism 9, and IC50 values were generated from best-fit curves. Data represent the mean ± SD.

Growth curves: Cells were plated in triplicate at a density of 2×10^5 cells/well for BT-474 and 1×10^5 cells/well for HCC1954 in 12-well plates. After 24h, cells were treated with control (rituximab 10 µg/mL or DMSO), trastuzumab (10 µg/mL), T-DM1 (0.1 µg/mL), DM1 (5 nM) or T-DXd (0.1 µg/mL). For time point 0 (24h after seeding), and subsequently for all other time points (day 2, day 4, day 6, and occasionally day 8),

cells were washed twice with PBS, trypsinized, counted using a hemocytometer and then treated again with fresh media containing the respective drugs.

Colony formation assay

Duplicates of 6 x 10^2 HCC1954^{WT} or HCC1954^{KO} and 1,2 x 10^3 BT-474^{WT} or BT-474^{KO} cells were plated in 12-well-plates and left undisturbed at 37°, 5%CO2 for 4 days. Then, cells were treated with vehicle (DMSO), Trastuzumab, T-DM1, DM1 or T-Dxd at the indicated concentrations for 21 days, with weekly change of spent media. At the end of treatment, cells were washed twice with ice-cold PBS and fixed with ice-cold methanol for 15 min. Afterwards, 0.5% crystal violet solution (Sigma V5265) was added to the plates and incubated at room temperature for 15 min. Plates were then washed with ddH2O, until the unbound crystal violet was removed and plates were dried at room temperature. Images were processed using the ColonyArea ImageJ plugin250.

RasG12V overexpression and active Ras pull-down

KRASG12V from pDONR223_KRAS_p.G12V (Addgene #81665) was cloned on the lentiviral backbone pLenti CMV hygro dest (Addgene #17454). HEK293T cell transfection and infection of target cells was performed by Calcium Chloride followed by hygromycin B (InvivoGen) 0.5 mg/mL selection for 8 days.
Levels of active Ras were determined using the Active Ras Detection Kit (#8821, Cell Signalling Technology). Briefly, cell lysates (500 µL at 1 mg/mL) were treated in vitro with GTPγS or GDP to activate or inactivate Ras, respectively. The lysates were then incubated with glutathione resin and GST-Raf1-RBD for 1h at 4°C, washed and the resulting RAS-RAF1 complexes eluted from the resin by boiling in 2X SDS sample buffer. Proteins were resolved by SDS-PAGE, transferred to nitrocellulose and western blot analysis (20 µL of the eluted samples) was performed using the anti-RAS antibody supplied by the manufacturer. An anti-mouse IgG, HRP-linked Antibody (#7076) was used as the secondary antibody.

Immunofluorescence and confocal microscopy

Internalisation assay: three batches of 7.5 x 10^5 BT-474 cells were seeded on 0.5% gelatin-coated coverslips and allowed do attach overnight. After a 15 min T-DM1 or T-DXd pulse (1.5 µg/mL), drugs were washed off and one batch of cells was immediately fixed with PFA 4% for 15 min RT and analysed for baseline membrane impregnation. The remaining batches received fresh warm media and were incubated at 37°C for 24 h, with or without chloroquine (CQ, 5 µM). Cell were then fixed as previously described and all three batches were permeabilised with Triton X-100 0.5% in PBS and a Cy5-conjugated anti-human (AC112S, Sigma) was used for the detection of T-DM1 and T-DXd; a FITC-phalloidin (P5282, Sigma) was used for actin and nuclear counterstaining was done with DAPI. Images were acquired with an SP8 confocal microscope (Leica Microsystems GmbH, Wetzlar, Germany) and a 63x/1.4NA oil immersion objective lens. Multichannel, Z-stack images were acquired with a voxel size of 72x72x200 nm3 by 3 different PMT detectors. To determine internalisation, single cells were segmented and the mean cytosol fluorescence signal of each single cell was evaluated (n = 28). Statistical analyses were performed using the Student's t-test, two-tailed.

Co-localization immunofluorescence: HCC1954 WT and KO cells were seeded (9 x 104 in 12-well plates) on coverslips coated with 0,5% gelatin and allowed to attach overnight. Cells were synchronized with RO3306 at 9µM for 20 hours. Cells were released from late G2 block and, after 1 hour, MG132 was added at 10µM. After 1 hour and half, cells were treated with cross-linker disuccinimidyl propionate (DSP, Thermo Scientific #A35393) at 1mM diluted in HBSS for 10 minutes at room temperature. Finally, cells were fixed with cold methanol at -20˚ C for 3 minutes, followed by rehydration in PBS-Tween0,1%. Fixed cells were then blocked with 5% Normal Donkey Serum (Jackson ImmunoResearch; code:017-000-121) + 0,3% Triton X-100 in PBS for 1 hour and subsequently incubated with primary antibody mouse anti-Neurofibromin (MilliporeSigma, NF1-A 376G3, #MABN2557) diluted 1:100 in IF buffer (1x TBS + 0,1% Triton X-100 + 2% BSA + 0,1% Sodium Azide in PBS) for 5 hours. NF1 primary antibody was detected using Alexa Fluor-555 secondary antibody (Life Technologies) incubated for 45 minutes. After 5 minutes crosslinking with 4% PFA, cells were incubated with primary antibody mouse anti-Tubulin Alexa Flour-488 conjugate (Cell Signaling

Technologies, clone DM1A, #8058) diluted 1:100 in IF buffer for 5 hours. DAPI (Sigma, D9542; 1:1000) was used for nucleic staining.

Competitive co-culture

Vectors: the Tet-Off-H2B-GFP lentiviral vector422 and the H2B-mCherry retroviral vector423 were kindly provided by N Roda (Department of Experimental Oncology, European Institute of Oncology, Milan) and used in the following co-culture experiments. Tet-Off-H2B-GFP lentiviral vector was transfected in HEK293T cells together with 3rd generation packaging plasmids pMD2.G, pRSV-REV, and pMDLg/pRRE; H2B-mCherry retroviral vector was transfected in Phoenix-AMPHO cells instead. Viral supernatants were collected 2-4 days post-transfection and filtered through 0.45 mm filters. Filtered supernatants were concentrated by ultracentrifugation at 22.000 rpm for 2h at 4°C with OptimaTM L-90K ultracentrifuge (Beckman Coulter) and stored at -80°C (never refrozen).

Competitive co-culture: HCC1954 WT cells were infected with Tet-Off-H2B-GFP lentiviral vector while HCC1954 KO cells were infected with H2B-mCherry retroviral vector. Multiplicity of infection (MOI) = 2 and 8 µg/mL of Polybrene (Sigma-Aldrich) were used in both cases. Infected cells were selected via fluorescence activated cell sorting (FACS) using a BD FACSAria II. Sorted cells were subsequently mixed 1:1 and allowed to grow for up to 5 days in the presence or absence of 0.1 µg/mL of T-DM1. At day 0 (plating), 3, and 5, co-cultures were investigated by FACS to determine the fraction of wt and NF1 KO cells. Doublets of cells and cells with abnormal morphology were excluded for the analysis.

Flow cytometry

BrdU was pulsed for 1 h on BT-474 and SK-BR-3 cells (WT and *NF1* KO) treated with T-DM1 or vehicle for 36 h. Cells were fixed and stained according to manufacturer's instructions (FITC BrdU Flow Kit, BD Biosciences). Samples were manually loaded, with acquisition criteria of 10.000 events or 3 minutes for each tube. During acquisition preview, gates for cells were adjusted in the FSC-A *vs* SSC-A plot, and the DNA 7-AAD-A voltage was adjusted to place the mean of the singlet peak (G0/G1) at 50.000 in the histogram. Cell cycle gates were adjusted as needed to encompass the G0/G1, S, and G2/M populations. Data was analyzed using FlowJo x.10.0.7r2 software (Tree Star).

To assess the effect of T-DM1 treatment on cell cycle distribution, harvested cells were fixed with 70% cold ethanol (Panreac Applichem) in PBS (Thermo Fisher Scientific), and stored at 4°C. After 8h, cells were centrifuged and resuspended in PBS (Thermo Fisher Scientific). DAPI (Sigma-Aldrich) was then added at the final concentration of 50 µM overnight at 4°C. Cell cycle distribution was analysed by FACS and differences in cell cycle distribution were evaluated through the $\chi 2$-test.

For HER2 expression analysis, 2 x 105 MDA-MB-231, BT-474 WT and KO cells were pelleted at 3000 rpm for 5 minutes. Cells were blocked with 5% BSA in PBS for 30 minutes and then incubated with primary antibody anti-HER2 Alexa Fluor-488 conjugate (#FAB1129G-025, Biotechne) diluted in 1% BSA in PBS for 1 hour at 4˚ C in agitation. Finally, cells were washed with 1% BSA in PBS and resuspended in 2% BSA in PBS). Flow cytometry was performed on BD FACS Celesta and all data were analysed using FlowJo 10.

Immunoblot analyses

Cells were lysed in RIPA buffer (150 mM NaCl; 1% NP-40; 0,5% Sodium deoxycholate, 0,1% SDS, 25mM Tris, pH 7.4 in ddH2O) supplemented with PhosSTOP (Roche) and protease inhibitors (Roche). A protein fraction was obtained by centrifuging at 10.000 × g for 20 min at 4 °C. Supernatant was collected and protein concentration was determined using the Pierce™ BCA protein assay kit following manufacturer's instructions (Thermo Fisher Scientific, Massachusetts, USA). Each sample was separated by non-reducing SDS-PAGE with Precision Plus Protein Dual Color Standards (Bio-Rad) and transferred to nitrocellulose membrane overnight at 4 °C. Where applicable, western blots were cut horizontally to allow the detection of different proteins within a single experiment. Blots presented in figure panels were derived from the same experiment and processed in parallel. The rest of the antibodies utilized here are: rabbit anti-cleaved PARP (Asp214, D64E10, XP® 5625); mouse anti-Bcl-2 (100/D5); mouse anti-GAPDH (6C5); rabbit anti-β-Tubulin (9F3); mouse anti-vinculin (A250291). Donkey anti-mouse IgG or goat anti-rabbit IgG secondary antibody conjugated to horse-radish peroxidase (Jackson ImmunoResearch Laboratories, Inc., Pennsylvania, USA) were probed against primaries 45 minutes at room temperature and detected bands were visualized

using ECL reagent (Novex™ ECL Chemiluminescent Substrate Reagent Kit, Thermo Fisher Scientific, Massachusetts, USA) and processed using Image LabTM software 6.0.1 (Bio-Rad).
F0r HER2 expression, MDA-MB-231, BT-474 and HCC1954 cells were lysed with RIPA buffer (150 mM NaCl, 1% Nonidet P-40, 0.5% Sodium deoxycholate, 0.1% SDS, 25mM Tris pH 7.4 in ddH_2O) supplemented with PhosSTOP (Roche) and protease inhibitors (Roche). A protein fraction was obtained by centrifuging at 13000 rpm for 20 min at 4°C. Supernatant was collected and protein concentration was determined using the PierceTM BCA protein assay kit following manufacturer's instructions (Thermo Fisher Scientific, Massachusetts, USA). Each sample was separated by non-reducing SDS-PAGE (6% acrylamide gel) with Precision Plus Protein Dual Color Standards (Bio-Rad) and transferred to nitrocellulose membrane overnight at 4 °C. The membrane was blocked with 5% BSA diluted in TBS-Tween0,1% for 1 hour and primary antibodies were incubated overnight (rabbit anti-HER2 #29D8 Cell Signaling; mouse anti-vinculin #A250291). Donkey anti-mouse IgG or goat anti-rabbit IgG secondary antibody conjugated to horse-radish peroxidase (Jackson ImmunoResearch Laboratories, Inc., Pennsylvania, USA) were probed against primaries 45 minutes at room temperature and detected bands were visualised using ECL reagent (NovexTM ECL Chemiluminescent Substrate Reagent Kit, Thermo Fisher Scientific, Massachusetts, USA) and processed using Image LabTM software 6.0.1 (Bio-Rad).

Single-cell fate analysis using FUCCI(Ca) cell cycle reporter

Model generation and data acquisition: Stable FUCCI-expressing model was generated by co-transfecting the pCSII-EF-MCS vector encoding the FUCCI(Ca)(Sakaue-Sawano et al., 2017) probe with the packaging plasmid (pCAG-HIVgp) and the VSV-G-/Rev-expressing plasmid (pCMV-VSV-G-RSVRev) into 293T cells. High-titer viral solutions were prepared and used for transduction into both WT and NF1 KO BT-474 cells by two rounds of infection of 4 viral particles per cell (MOI 1) followed by flow cytometry-based sorting (FACSAria cell sorter, BD). For live cell imaging, 0.5 x 10^5 cells were seeded in µ-Slide 8-well glass bottom chambers (80827, Ibidi). Twenty-four hours later, T-DM1 or control (rituximab, targeting the CD19 antigen not expressed on target cells) were added at the indicated concentrations 30 minutes before starting acquisition. Images were acquired with a Spinning Disk Confocal Microscope (Nikon) at 10x for 90h.
Database generation: for each experimental condition, we tracked cells in the mCherry (Red,R) and mVenus (Green,G) channels using TrackMate 7.2.0 on nine different fields of view (FoV), for a maximum of 530 frames, 10 min apart from each other, over 90h. Only cells that remained alive for at least 12h were followed by the tracker. For those, intensities on both channels were measured for each time frame starting from time 0 (T0).
Pre-processing: we first removed cells showing channel intensities lower than 200 for all the observed time lapse. Then, we applied a sliding average (window width = 5 points) to reduce noise and to smooth intensity signaling.
Algorithm to identify cell cycle phase: Using the sliding average values of both channel intensities for a cell of interest as input, we identified the cell cycle phase (G1, S, G2/M) and the "Lost by the tracker" condition ("Lost") for each time point in the observed time lapse.

The first step is the identification of preliminary G1 and S frames, considering the channel intensities: if Red(x_i)>Green(x_i), the frame x_i at time point i is classified as G1, otherwise as S.
Integrating the behaviour of channel intensities with tracker movies, we observed that the G2/M phase corresponds to a sharp increase in the mCherry (R) channel intensity when the cell is still in the S phase, matching to a decrease in the mVenus (G) channel intensity. The G2/M phase stops whit a sharp decrease of the G channel intensity coupled with an increase in the R channel intensity, which determines the G1 entry. We thus set several rules to identify G2/M frames, studying the derivatives of red and green intensities for each frame x_i ($d_{red}(x_i)$ and $d_{green}(x_i)$).

We classified as G2/M the frames x_j where:

- $d_{red}(x_i)$ >1 and x_j was previously classified as S. To avoid the identification of small fluctuation as G2/M, we selected only groups of consecutive frames longer than 6 (equivalent to an hour) or, if none of those sequence is available, we selected only the longest sequence of consecutive frames;

- $d_{red}(x_{i-1})<1$ and i is the last available time point;
- $d_{green}(x_i) < (-5)$ and x_i was previously classified as G1;
- $d_{green}(x_i) < (-1)$ with x_i previously classified as S and $i > j$ where $j = \max_k \quad x_k$ such that $x_k$is classified as G2/M
- both Red(x_i) and green(x_i) were higher than 200

After that, each frame is classified as G2/M, S or G1. We then checked frame by frame whether the order of phases in the cell cycle (G1 then S then G2/M) was respected. Residual misclassifications were further fixed with the following set of rules:

- in G2/M-S-S sequences, the first S is replaced by G2/M
- in G2/M-S-G2/M sequences, S is replaced by G2/M
- in G1-G2/M sequences, g2/m is replaced by G1
- in G1-S-G1sequences, S is replaced by G1

We then identified frames lost by the tracker, considering fluctuations in the ratio between the sliding averages of mCherry and mVenus channel intensities. This value should remain constant for dying cells: a coefficient of variation (CV) >0.1 on a sliding average (window width=7 points) was used to identify fluctuations.
We identified the last frame x_m with CV>0.1: all its consecutive frames (x_j, j>m) with a percentage of Red intensity ($\frac{red(x_j)}{red(x_j)+green(x_j)} \cdot 100$) >80% and dred($x_j$)<0.5 were identified as Lost, unless they had red(x_j)≥200 or unless they were preceded by a S frame with increasing dred(x_j).
We also set as Lost the last available frame if the previous one was defined as Lost.
Finally, to remove fluctuations, spurious "Lost" frames were reclassified as in the first part of the algorithm, while we forced spurious not "Lost" frames in assessed "Lost" sequences to the "Lost" class.
Analysis of identified cell cycle phases: we applied our algorithm to all the available FoV for each condition. Once we assigned a phase to each frame, we dissected the complete cell cycles identified. To plot the cell phases story (Figure 2i) we excluded cells whose first frame was classified as G2/M, in order to only include cells whose G2/M phase could be monitored from beginning to end. We compared the percentage of frames assigned to the G2/M phase in NF1 KO cells (vehicle, T-DM1 0.1µg/mL and T-DM1 1µg/mL) with the corresponding percentage in the WT population. We performed a Wilcoxon test for statistical analysis, with significance at 0.05.
We also considered the frequency of cell transitions between different phases and compared them across conditions with a Chi-squared test.

CETSA melting curves
Growing BT-474 cells were harvested, washed once with PBS, and diluted in Hanks' Balanced Salt Solution (HBSS, Thermo Fisher Scientific) supplemented with PhosSTOP (Roche) and protease inhibitors (Roche) to 4 x 106 cells/mL. The cell suspension was then mixed with DMSO or DM1 1 µM and kept on a wheel at 37°C for 2.5 h before aliquoting into PCR-tubes. Melting curves were generated by heating samples for 3 min in a Veriti Thermal cycler (Applied Biosystems) at the following stepwise temperature range: 57°C, 59°C, 61°C, 63°C, 65°C, 67°C. Cells were subsequently lysed with three rounds of freeze-thaw by alternating exposure of the samples to liquid nitrogen and 20°C in a PCR-machine. Samples were then resolved by SDS-PAGE gel, transferred to nitrocellulose and analyzed by immunoblotting against b-tubulin (9F3). For the quantitative analysis, we first normalized mean band intensities obtained for temperatures within our range on the mean band intensity obtained at the starting temperature (57°C), considering the treatment (DMSO or DM1). To understand which factors affected most the differences observed in figure 8, we performed a two-way ANOVA separately for BT-474WT and BT-474KO normalized data. We considered as factors the treatment, the temperature and their combination.

Chromosome misalignment analysis and centriolar quantification

BT-474 WT and BT-474 KO cells were seeded as per internalization assay. After 24h, cells were synchronized with RO3306 (Sigma-Aldrich) at 9 µM for 39 or 22.5h, respectively (half their doubling time) at 37°C. Cells were then washed three times with warm media for late G2 block release and put back at 37°C. After 50 min, cells were treated with MG-132 (Tocris) 10 µM for 90 min at 37°C. Finally, cells were fixed either by immersion in cold methanol at -20°C for 4 min followed by rehydration in PBS for 10 min or with 4% paraformaldehyde (PFA) for 15 min followed by permeabilization with 0.5% Triton X-100 for 20 min. For double thymidine block (DTB), SK-BR-3 cells were grown to a 40% confluence instead and 2 mM of thymidine was added. After incubation at 37°C for 18h, cells were washed with PBS and put back in culture with fresh media for 9h. After that, thymidine was added again for another 15h. Cells were then washed three times with warm media for release and fixed after 8h with 4% paraformaldehyde. Fixed cells were all blocked with 3% BSA for 1h and incubated in primary antibodies diluted in PBS-Tween20 0.1%, 3% BSA and 0.02% NaN_3. Primary antibodies used for immunofluorescence (IF) analysis included mouse anti-a-tubulin (T5168), human anti-centromere protein (15-234), rabbit anti-phospho-histone H3(Ser10) (06-570), and rabbit anti-CEP63 (06-1292). Primary antibodies were detected using Alexa Fluor-labelled secondary antibodies (Life Technologies) while DAPI (D9542) was used for nucleic staining. Coverslips were mounted using Mowiol and images were acquired as previously reported. Cell phenotypes were scored visually by counting non-overlapping FoVs in a raster scan pattern across the coverslip.

Chromosomal and microtubular dynamics during mitosis

BT-474WT-H2B-GFP and BT-474KO-H2B-mCherry cells were seeded (40 x 10^3 cells) in µ-Slide 8-well glass bottom chambers (80827, Ibidi). Twenty-four hours later, growing cells were stained for 1.5h before acquisition with the SiR-tubulin probe (#SC002, Spirochrome; λabs 652 nm/λfl 674 nm) at 1 µM. Time-lapse microscopy was performed using an inverted microscope (Nikon Eclipse Ti) with a 20X objective. The microscope was equipped with an incubation chamber maintained at 37°C in an atmosphere of 5% CO2 and acquisitions were made every 4 min. A total of 28 cells were analysed for BT-474 WT and 38 for BT-474 KO.

Immunofluorescence and high-resolution confocal microscopy

BT-474 and SK-BR-3 cells were seeded on coverslips coated with gelatin 0,5% and allowed do attach overnight. Cells were synchronized with RO3306 at 9µM for 36 and 16h, respectively. T-DM1/maytansine or vehicle were added at the last 12h on the indicated concentrations. Cells were released from late G2 block and, after 50 minutes, MG132 was added at 10µM. Then, cells were fixed either by immersion in cold methanol at -20°C for 6 min followed by rehydration in PBS for 10 min or by fixing with 4% paraformaldehyde in PBS for 10 min followed by permeabilization with 0.5% Triton X-100 in PBS for 20 min. Fixed cells were then blocked with 3% BSA in PBS for 1 h and incubated in primary antibodies diluted in PBS-Tween20 0,1%, 3% BSA and 0,02% NaN_3. Primary antibodies used for immunofluorescence analysis included rabbit anti-CEP63 (Merck, 06-1292; 1:1000), mouse anti-a-tubulin antibody (Sigma, T5168; 1:1000), human anti-centromere protein (Antibodies Incorporated, 15-234; 1:1000), rabbit anti-phospho-histone H3(Ser10) (Merck, 06-570; 1:500). Primary antibodies were detected using Alexa Fluor-labelled secondary antibodies (Life Technologies) while DAPI (Sigma, D9542; 1:5000) was used for nucleic staining. Cells were imaged with an SP8 confocal microscope (Leica Microsystems GmbH, Wetzlar, Germany) and a 63x/1.4NA oil immersion objective lens. Multichannel, Z-stack images were acquired with a voxel size of 72x72x200 nm^3 by 3 different PMT detectors. Cell phenotypes were scored visually by counting non-overlapping FoVs in a raster scan pattern across the coverslip. Eight-bit images were exported, and figures were prepared using Affinity Designer (Serif, West Bridgford, UK). Image data were quantified using ImageJ, and graphical representations and statistical analyses were performed using Graphpad Prism 9.1.1.

Co-localization immunofluorescence

HCC1954 WT and KO cells were seeded (9 x 10^4 in 12-well plates) on coverslips coated with 0,5% gelatin and allowed to attach overnight. Cells were synchronized with RO3306 at 9µM for 20 hours. Cells were released from late G2 block and, after 1 hour, MG132 was added at 10µM. After 1 hour and half, cells were treated with cross-linker disuccinimidyl propionate (DSP, Thermo Scientific #A35393) at 1mM diluted in HBSS for 10 minutes at room temperature. Finally, cells were fixed with cold methanol at -20˚ C for 3 minutes, followed by rehydration in PBS-Tween0,1%. Fixed cells were then blocked with 5% Donkey Serum

+ 0,3% Triton X-100 in PBS for 1 hour and subsequently incubated with primary antibody mouse anti-Neurofibromin (MilliporeSigma, NF1-A 376G3, #MABN2557) diluted 1:100 in IF buffer (1x TBS + 0,1% Triton X-100 + 2% BSA + 0,1% Sodium Azide in PBS) for 5 hours. NF1 primary antibody was detected using Alexa Fluor-555 secondary antibody (Life Technologies) incubated for 45 minutes. After 5 minutes crosslinking with 4% PFA, cells were incubated with primary antibody mouse anti-Tubulin Alexa Flour-488 conjugate (Cell Signaling Technologies, clone DM1A, #8058) diluted 1:100 in IF buffer for 5 hours. DAPI (Sigma, D9542; 1:1000) was used for nucleic staining.

NF1 expression and purification:
the NF1 isoform 1 recombinant protein was produced in insect cells starting from the plasmid R702-X38-635 encoding for His6-Hs.NF1opt (1-2839) (a gift from Dominic Esposito; http://n2t.net/addgene:159576; RRID:Addgene_159576) [33]. The vector was further modified by mutagenesis (GeneScript) by inserting a Prescission cleavage site between the His-tag and the NF1 coding sequence. The protein was expressed by infection of High Five Cells (BTI-TN-5B1-4) (ThermoFischer Scientific) with the baculovirus obtained from the above-mentioned vector. Cell pellets were resuspended in lysis buffer (25 mM Hepes pH 7.5, 500 mM NaCl, 5% Glycerol, 1 mM DTT) supplemented with protease inhibitors cocktail Set III (Calbiochem) and DNAseI (PanReac AppliChem), lysed mechanically by dounce homogenizer and cleared by centrifugation at 70000 g for 45 min at 4°C. The supernatant was filtered through 0.22 µm filter (sartorius) and then loaded on a 5 ml HisTrap HP column (Cytiva) using an AKTA chromatography system. The column was washed with a buffer containing 38 mM imidazole and the protein was then eluted with a buffer containing 250 mM. The resulting sample was incubated overnight at 4°C with recombinant Prescission protease at a protein:protease ratio of 100:1 (w/w), to cut the His-tag. After cleavage, the protein was concentrated and loaded on a Superose 6 column (Cytiva) pre-equilibrated in SEC buffer (25 mM Hepes pH 7.5, 300 mM NaCl, 5% Glycerol, 1 mM DTT). Fractions containing monodisperse protein were concentrated in a 100 kDa cut-off Amicon ultra centrifugal filters (Millipore) and flash frozen in liquid nitrogen for further assays. Protein concentration was determined by measuring sample absorbance at 280nm using the extinction coefficient calculated from the amino acid sequence.

Mass photometry: NF1 molecular mass was measured at a final concentration of 10nM in 25mM Hepes pH7,5, 300mM NaCl, 5% Glycerol, 1mM DTT with the TwoMP instrument (Refeyn).

GAP-stimulated GTPase activity assay: We tested the functionality of our purified NF1 by evaluating its RAS-GAP activity through the GTPase-Glo™ assay (Promega), a bioluminescent assay that quantitates the amount of GTP remaining after a GTPase reaction. Reactions were assembled with 2µM Ras and 1µM NF1 in GTPase/GAP Buffer provided by the kit. Reactions were initiated by adding 5µl of 10µM GTP in GTPase/GAP Buffer containing 1mM DTT. The final reaction volume was 10µl. Reactions were incubated for 90 minutes at room temperature. To the completed GTPase reactions, 10µl of GTPase-GloTM Reagent was added and reactions were incubated for 30 minutes at room temperature. Twenty microliters of Detection Reagent were added, plates were incubated for 5–10 minutes at room temperature and luminescence was recorded using the GloMax®-Multi+ Detection System.

Co-sedimentation assay: 20µM Tubulin (Cytoskeleton Inc) was polymerized into stable Microtubules in General Tubulin Buffer (80 mM PIPES pH 6.8, 1 mM MgCl2, 1 mM EGTA), supplemented with 1 mM GTP and 50 µM Paclitaxel at 37°C for 20 minutes. For Microtubule-binding reactions, Microtubules were diluted to a final concentration of 9µM in General Tubulin Buffer supplemented with 1 mM GTP, 50µM Paclitaxel and 60mM NaCl. 0,6 µM NF1 and 5 µM NuMA proteins were added to a final volume of 50µl. Reactions were incubated at room temperature for 15 minutes, transferred onto 100 µl of cushion buffer (80 mM PIPES pH 6.8, 1 mM MgCl2, 1 mM EGTA, 50 µM Paclitaxel, 50 % glycerol) and ultracentrifuged for 15 minutes at 400,000 g at 25 °C in a Beckman TLA100 rotor. The supernatant (50µl) was transferred from each centrifuge tube in SDS loading buffer. The cushion buffer was discarded very gently. The pellet was resuspended in SDS loading buffer 1x. Pellets and supernatants were analysed by SDS-PAGE.

Tubulin polymerization assay: Microtubules turbidity assay is based on adaptation of the original method of Shelanski et al.[14] and Lee et al.[15] which demonstrate that the light scattered by microtubules is directly proportional to the concentration of microtubule polymer. As dimers assemble into polymers, the solution scatters more light, which can be detected by the increased optical density measurable by a spectrophotometer[16]. Tubulin polymerizes with characteristic kinetics including a lag phase indicative of nucleation, a log phase indicative of polymerization, and a steady-state phase indicative of no net polymer growth. Briefly, 3mg/mL Tubulin was mixed on ice in a 96 well plate with 0,6µM NF1 or 10µM Paclitaxel (positive control) or 10µM Nocodazole (negative control) in a final volume of 100µL in Tubulin Polymerization Buffer (80 mM PIPES pH 6.9, 2mM MgCl2, 0.5mM EGTA, 1mM GTP, 10% glycerol). The polymerization reaction was started by the increase in temperature from 4°C to 37°C upon transfer of the reaction to pre-warmed microtiter spectrophotometer. Tubulin assembly was monitored for one hour at 340nm in kinetic mode of 61 cycles for each sample and the readings were recorded at an interval of 1 min (Infinite 200 PRO-Tecan plate reader).

Microtubule dynamics measurement

Microtubules

Porcine brain tubulin was isolated using the high-molarity PIPES procedure[44,45]. Biotin-labeled tubulin as well as HiLyte647-labeled tubulin and TAMRA Rhodamine labeled tubulin were purchased from Cytoskeleton Inc. (T333P, TL670M and TL590M respectively).

GMPCPP-lattice microtubules (GMPCPP polymerized) were polymerized from 4 mg/ml HiLyte-647-labeled biotinylated pig-brain tubulin (12% biotin tubulin, 20% HyLite647-labeled tubulin, 68% unlabelled tubulin) for 1 h at 37 □C in BRB80 supplemented with 2.7 mM GMPCPP (Jena Bioscience, NU-405). The polymerized microtubules were centrifuged for 30 min at 18000 x g in a Microfuge 18 Centrifuge (Beckman Coulter). After centrifugation the pellet was resuspended in BRB80.

TIRF microscopy

Total internal reflection fluorescence (TIRF) microscopy experiments were performed on an inverted microscope (Nikon Eclipse Ti-E) equipped with 60x oil immersion objectives (Apo TIRF, Nikon) and Hamamatsu Orca Flash 4.0 CMOS camera. An additional 1.5x magnifying tube lens was used. Hilyte-647-labeled biotinylated microtubules and TAMRA Rhodamine labelled tubulin were visualized sequentially by switching between microscope filter cubes for Cy5 and mCherry channels. The imaging setup was controlled by NIS Elements software (Nikon).

Flow chambers for TIRF imaging assays were prepared as described previously (1). Channels were treated with anti-biotin antibody solution (Sigma, B3640, 1 mg/ml in PBS) after 5 minutes, followed by one-hour incubation with 1% Pluronic F127 (Sigma, P2443).

Microtubule dynamics assay

To determine how microtubules grow in the presence of NF1/DM1 and DM1 with NF1 together and GTP we employed microtubule dynamic assay. We first mobilized microtubule Hilyte-647- labelled biotinylated microtubules and subsequently flushed in the assay buffer (BRB80, 1 mM GTP, 0.2% Tween20, 0.5 mg/ml Casein, 20 mM D-glucose, 0.22 mg/ml glucose oxidase and 20 ug/ml catalase) with free 20 µM HyLite-647 tubulin in the absence or presence of 100 nM NF1/1 µM DM1/ 300 nM NF1 with 1 µM DM1. Time-lapse image sequences were recorded for 20 min at the rate of 1 frame per 10 s with an exposure time 100 ms. Data from three independent experiments was collected, each experiment was repeated at least on three days.

Image analysis

Microscopy data were analyzed using ImageJ (FIJI). Dynamic parameters of microtubules in the presence of NF1/ DM1/ NF1 with DM1. Dynamic instability parameters microtubules as polymerization rate, depolymerization rate, frequency of catastrophes and frequency of rescues was analysed using Kymographs, which were generated using KymographBuilder plug-in In FIJI by manually fitting lines along the A- and B-microtubules.

RNA-seq

mRNA-seq libraries were prepared according to the TruSeq low sample protocol (Illumina, San Diego, CA, USA), starting with 1 µg of total RNA per sample. RNA-seq libraries were pair-end sequenced on an Illumina NovaSeq 6000 sequencing platform. RNA-seq data were mapped using the STAR aligner version 2.7.1a against the human genome (hg19) .Read counts were calculated with htseq-counts with the standard UCSC reference GFF (https://hgdownload.soe.ucsc.edu/goldenPath/hg19/bigZips/genes/hg19.refGene.gtf.gz). Differential expression analysis was done with DESeq2 R package version 1.36.0. Genes of interest were selected using a false discovery rate (FDR) cut-off of $1x10^{-4}$

Functional enrichment analysis war performed using EnrichR R package version 3.1 on differentially expressed genes with log2foldchange < -1 in NF1 knock-out T-DM1 treated vs NF1 knock-out and log2foldchange > -1 and log2foldchange < 1 in wild-type T-DM1 treated vs wild-type. Queries were performed over four different molecular signatures: Gene Ontology Biological Process, Gene Ontology Molecular Function, Gene Ontology Cellular Component (https://www.gsea-msigdb.org/gsea/msigdb/download_file.jsp?filePath=/msigdb/release/2022.1.Hs/c5.go.v2022.1.Hs.symbols.gmt) and Hallmark (https://www.gsea-msigdb.org/gsea/msigdb/download_file.jsp?filePath=/msigdb/release/2022.1.Hs/h.all.v2022.1.Hs.symbols.gmt) (10.1073/pnas.0506580102, 10.1093/bioinformatics/btr260, 10.1016/j.cels.2015.12.004). Enriched terms were selected using a standard FDR cut-off of $1x10^{-2}$.

Arm-level Aneuploidy Assessment

GENIE data were retrieved from GENIE cbioportal webserver version 13.0 (https://genie.cbioportal.org/) selecting breast cancer sample (15210). We selected samples that had been sequenced with the following panels that contain the NF1 gene: MSK-IMPACT341, MSK-IMPACT410, MSK-IMPACT468, GRCC-MOSC3, UCSF-NIMV4-TN, UCSF-NIMV4-TO reducing the sample size to 6598 samples. Of this 58 are NF1 mutated. NF1 mutated samples were selected using the following criterium: samples with truncating mutations (frameshift insertion/deletion, non-sense mutations, canonical splice-site variants) or samples with missense mutations predicted "pathogenic" by the functional predictor AlphaMissense [32]

Aneuploidy scores (AS) were quantified on segmentation data downloaded from cBioPortal using ASCETS (Arm-level Somatic Copy-number Events in Targeted Sequencing), a targeted-sequencing specific aneuploidy score quantifier[30]. ASCETS was run using UCSC cytoband coordinates (reference build hg19) provided in the ASCETS github repository (https://github.com/beroukhim-lab/ascets/blob/master/cytoband_coordinates_hg19.txt). AS was calculated with standard parameters with a minimum breadth of coverage of 0.5 and alteration threshold of 0.7.

NF1 Mutated Patients Prevalence

To assess mutational prevalence of NF1 were selected two cohorts: i) GENIE (Genomics Evidence Neoplasia Information Exchange) cohort database (v13.0-public) and ii) TCGA PanCancer Genome Atlas (2018) Breast Cancer Cohort (10.1038/ng.2764).

Only patients with breast cancer were selected. Subsequently the cohorts were divided into two subcategories ERBB2 amplified and ERBB2 wilt-type.

TCGA PanCancer Genome Atlas Breast Cancer Cohort was used to select primary samples; GENIE cohort was used to selected metastatic samples.

Odds ratio were calculated as the ratio of gene frequencies in metastatic versus primary cohorts. Genes with less than 5% of mutated samples, considered poorly informative, were excluded to avoid false-negatives FDR overcorrection.

NF1 lollipop plots have been designed using ProteinPaint (https://pecan.stjude.cloud/proteinpaint).

Mouse xenograft models

Engineering of Luc-tagged HCC1954 cells (HCC1954-Luc) and tumour implantation: the pLenti CMV Puro LUC (w168-1) was purchased from Addgene (#17477) and used in all in vivo experiments. This 3rd generation lentiviral vector allows for the constitutive expression of firefly luciferase under the CMV promoter. The vector also contains genes that encode for puromycin and ampicillin resistance. Both

HCC1954^{WT} and HCC1954^{KO} cells were transduced with the pLenti CMV Puro LUC reporter vector at MOI = 5 in the presence of 8 µg/mL of Polybrene (Sigma-Aldrich). Infected cells were selected by puromycin (2.5 µg/mL for 72h; Vinci-Biochem) and allowed to expand for additional 8 days post selection. Tumours were implanted in 9-week-old NOD scid γ (NSG) mice, acquired from Charles River Laboratories) by intra-fat pad orthotopic injection of 106 HCC1954WT-Luc on the 9th mammary gland – left; and 106 HCC1954KO-Luc on the 5th - right) resuspended in sterile PBS (Thermo Fisher Scientific) and pre-mixed at a 1:1 dilution with growth-factor-reduced Matrigel (Corning) in a total volume of 30 µL. Tumour volume was weekly assessed via bioluminescence imaging (BLI) (IVIS-Lumina, Perkin Elmer). On day 14, once tumours were palpable (≥4 mm3), mice received a single intravenous injection of 4 mg/kg T-DM1 or NaCl 0.9%. Mice were weighed when cells were implanted (Day 0) and then twice weekly during the study. Experiment was terminated after 35 days.

Bioluminescence imaging (BLI) acquisition and analysis: the images were acquired using PerkinElmer's IVIS Lumina Series III instrument wavelengths (600- 800 nm). Scans were taken with an integrated CCD camera (Andor, Belfast, UK) supercooled down to −80 °C, with a 25 mm focal length lens (Navitar, Rochester, NY). The camera pointed straight down and was focused 10 mm above the imaging membrane. The F-number was kept at f/0.95 throughout the study. Prior to imaging, 200 µL of D-Luciferin (10 mg/mL, XenoLight, Perkin Elmer) were injected intraperitoneally and mice were anesthetized in induction chambers with 1-4% isofluorane. With animals in the supine position, BLI images were acquired after 10 min after luciferin injection. An exposure time of 2s and binning of 4 was used at the beginning of the study, and imaging parameters were updated as the tumours became brighter throughout the study, in order to maximize sensitivity of bioluminescence and avoid pixel saturation. Tumour burden was represented as total flux (photons/s), which is average radiance (flux per unit area and unit solid angle) integrated over the region of interest, using the Living Image v4.7.3 in vivo software package (Perkin Elmer Inc).

Statistical methods

Statistical differences on continuous dependent variables were based on two-tailed t-tests, after assessment of distribution normality via the Shapiro test. When at least one of the continuous variables was not normally distributed, significance was based on Wilcoxon test. Significance was considered at pvalue≤0.05.

In cases in which independent categorical variables had more than 2 values, we applied 1- or 2-way ANOVA, according to the number of independent categorical variables used and then applied Tukey's HSD test to identify pairwise statistically significant differences. When time was one of the used variables, we instead performed a 3-way ANOVA with repeated measurements, followed by a post-hoc pairwise t-test. When the normality distribution hypothesis was not met, we applied Kruskal-Wallis with Dunn post-hoc test. In all those cases, given the small number of simultaneous hypotheses, a simple Bonferroni correction was performed (significance: adjusted pvalue<0.05).

Statistical differences in count distribution among categorical conditions were tested with Fisher's exact test (variables with>2 factors) or with Chi-squared test in cases where the variables had more than 2 factors. Significance was considered at pvalue≤0.05.

Specific statistical tests for complex data are described in the relative method section.

References

1. Marchuk, D. A. *et al.* cDNA cloning of the type 1 neurofibromatosis gene: complete sequence of the NF1 gene product. *Genomics* **11,** 931–940 (1991).
2. Philpott, C., Tovell, H., Frayling, I. M., Cooper, D. N. & Upadhyaya, M. The NF1 somatic mutational landscape in sporadic human cancers. *Hum. Genomics* **11,** 13 (2017).
3. Razavi, P. *et al.* The Genomic Landscape of Endocrine-Resistant Advanced Breast Cancers. *Cancer Cell* **34,** 427–438.e6 (2018).
4. Smith, A. E. *et al.* HER2 breast cancers evade anti-HER2 therapy via a switch in driver pathway. 1–10 doi:10.1038/s41467-021-27093-y
5. Zheng, Z.-Y. *et al.* Neurofibromin Is an Estrogen Receptor-α Transcriptional Co-repressor in Breast Cancer. *Cancer Cell* **37,** 387–402.e7 (2020).

6. Ratner, N. & Miller, S. J. A RASopathy gene commonly mutated in cancer: The neurofibromatosis type 1 tumour suppressor. *Nat. Rev. Cancer* **15,** 290–301 (2015).
7. Bollag, G. *et al.* Loss of NF1 results in activation of the Ras signaling pathway and leads to aberrant growth in haematopoietic cells. *Nat. Genet.* **12,** 144–148 (1996).
8. Chaker-Margot, M. *et al.* Structural basis of activation of the tumor suppressor protein neurofibromin. *Mol. Cell* **82,** 1288–1296.e5 (2022).
9. Gutmann, D. H., Wood, D. L. & Collins, F. S. Identification of the neurofibromatosis type 1 gene product. *Proc. Natl. Acad. Sci. U. S. A.* **88,** 9658–9662 (1991).
10. Lupton, C. J. *et al.* The cryo-EM structure of the human neurofibromin dimer reveals the molecular basis for neurofibromatosis type 1. *Nat. Struct. Mol. Biol.* **28,** 982–988 (2021).
11. Naschberger, A., Baradaran, R., Rupp, B. & Carroni, M. The structure of neurofibromin isoform 2 reveals different functional states. *Nature* **599,** 315–319 (2021).
12. Gregory, P. E. *et al.* Neurofibromatosis type 1 gene product (neurofibromin) associates with microtubules. *Somat. Cell Mol. Genet.* **19,** 265–274 (1993).
13. Koliou, X., Fedonidis, C., Kalpachidou, T. & Mangoura, D. Nuclear import mechanism of neurofibromin for localization on the spindle and function in chromosome congression. *J. Neurochem.* **136,** 78–91 (2016).
14. Bodakuntla, S., Jijumon, A. S., Villablanca, C., Gonzalez-Billault, C. & Janke, C. Microtubule-Associated Proteins: Structuring the Cytoskeleton. *Trends Cell Biol.* **29,** 804–819 (2019).
15. Gazzola, M. *et al.* Microtubules self-repair in living cells. *Curr. Biol.* **33,** 122–133.e4 (2023).
16. Triclin, S. *et al.* Self-repair protects microtubules from destruction by molecular motors. *Nat. Mater.* **20,** 883–891 (2021).
17. Aher, A. *et al.* CLASP Mediates Microtubule Repair by Restricting Lattice Damage and Regulating Tubulin Incorporation. *Curr. Biol.* **30,** 2175–2183.e6 (2020).
18. Lawrence, E. J., Arpag, G., Arnaiz, C. & Zanic, M. SSNA1 stabilizes dynamic microtubules and detects microtubule damage. *Elife* **10,** e67282 (2021).
19. Steinmetz, M. O. & Prota, A. E. Microtubule-Targeting Agents: Strategies To Hijack the Cytoskeleton. *Trends Cell Biol.* **28,** 776–792 (2018).
20. Tarantino, P. *et al.* Antibody–drug conjugates: Smart chemotherapy delivery across tumor histologies. *CA. Cancer J. Clin.* **72,** 165–182 (2022).
21. von Arx, C. *et al.* The evolving therapeutic landscape of trastuzumab-drug conjugates: Future perspectives beyond HER2-positive breast cancer. *Cancer Treat. Rev.* **113,** (2023).
22. Cabanillas, F. *et al.* Phase I study of maytansine using a 3-day schedule. *Cancer Treat. Rep.* **62,** 425–428 (1978).
23. Verma, S. *et al.* Trastuzumab Emtansine for HER2-Positive Advanced Breast Cancer. *N. Engl. J. Med.* **367,** 1783–1791 (2012).
24. Prota, A. E. *et al.* A new tubulin-binding site and pharmacophore for microtubule-destabilizing anticancer drugs. *Proc. Natl. Acad. Sci. U. S. A.* **111,** 13817–13821 (2014).
25. Lopus, M. *et al.* Maytansine and cellular metabolites of antibody-maytansinoid conjugates strongly suppress microtubule dynamics by binding to microtubules. *Mol. Cancer Ther.* **9,** 2689–2699 (2010).
26. Oroudjev, E. *et al.* Maytansinoid-Antibody Conjugates Induce Mitotic Arrest by Suppressing Microtubule Dynamic Instability. *Mol. Cancer Ther.* **9,** 2700–2713 (2010).
27. Cerami, E. *et al.* The cBio Cancer Genomics Portal: An Open Platform for Exploring Multidimensional Cancer Genomics Data: Figure 1. *Cancer Discov.* **2,** 401–404 (2012).
28. Gao, J. *et al.* Integrative Analysis of Complex Cancer Genomics and Clinical Profiles Using the cBioPortal. *Sci. Signal.* **6,** pl1 LP-pl1 (2013).
29. Sakaue-Sawano, A. *et al.* Genetically Encoded Tools for Optical Dissection of the Mammalian Cell Cycle. *Mol. Cell* **68,** 626–640.e5 (2017).
30. Spurr, L. F. *et al.* Quantification of aneuploidy in targeted sequencing data using ASCETS. *Bioinformatics* **37,** 2461–2463 (2021).
31. AACR Project GENIE Consortium. AACR Project GENIE: Powering Precision Medicine through an International Consortium. *Cancer Discov.* **7,** 818–831 (2017).
32. Cheng, J. *et al.* Accurate proteome-wide missense variant effect prediction with AlphaMissense. *Science (80-.).* **381,** eadg7492 (2023).
33. Sherekar, M. *et al.* Biochemical and structural analyses reveal that the tumor suppressor neurofibromin (NF1) forms a high-affinity dimer. *J. Biol. Chem.* **295,** 1105–1119 (2020).
34. Zhu, Z. C. *et al.* Interactions between EB1 and microtubules: dramatic effect of affinity tags and evidence for cooperative behavior. *J. Biol. Chem.* **284,** 32651–32661 (2009).
35. Stepanova, T. *et al.* Visualization of microtubule growth in cultured neurons via the use of EB3-GFP (end-binding protein 3-green fluorescent protein). *J. Neurosci. Off. J. Soc. Neurosci.* **23,** 2655–2664 (2003).

36. Janke, C. & Montagnac, G. Causes and Consequences of Microtubule Acetylation. *Curr. Biol.* **27,** R1287–R1292 (2017).
37. Xu, H. & Gutmann, D. H. Mutations in the GAP-related domain impair the ability of neurofibromin to associate with microtubules. *Brain Res.* **759,** 149–152 (1997).
38. Bollag, G., McCormick, F. & Clark, R. Characterization of full-length neurofibromin: tubulin inhibits Ras GAP activity. *EMBO J.* **12,** 1923–1927 (1993).
39. Replogle, J. M. *et al.* Aneuploidy increases resistance to chemotherapeutics by antagonizing cell division. *Proc. Natl. Acad. Sci. U. S. A.* **117,** 30566–30576 (2020).
40. Bakhoum, S. F. *et al.* Chromosomal instability drives metastasis through a cytosolic DNA response. *Nature* **553,** 467–472 (2018).
41. Pearson, A. *et al.* Inactivating NF1 Mutations Are Enriched in Advanced Breast Cancer and Contribute to Endocrine Therapy Resistance. *Clin. Cancer Res.* **26,** 608 LP-622 (2020).
42. Ly, N. *et al.* αTAT1 controls longitudinal spreading of acetylation marks from open microtubules extremities. *Sci. Rep.* **6,** 35624 (2016).
43. Acerbi, I. *et al.* Human breast cancer invasion and aggression correlates with ECM stiffening and immune cell infiltration. *Integr. Biol. (Camb).* **7,** 1120–1134 (2015).
44. Castoldi, M. & Popov, A. V. Purification of brain tubulin through two cycles of polymerization-depolymerization in a high-molarity buffer. *Protein Expr. Purif.* **32,** 83–88 (2003).
45. Gell, C. *et al.* Purification of tubulin from porcine brain. *Methods Mol. Biol.* **777,** 15–28 (2011).
46. Guzmán, C., Bagga, M., Kaur, A., Westermarck, J. & Abankwa, D. ColonyArea: An ImageJ plugin to automatically quantify colony formation in clonogenic assays. *PLoS One* **9,** 14–17 (2014).
47. de Forges, H., Pilon, A., Poüs, C. & Perez, F. in 139–153 (2013). doi:10.1016/B978-0-12-407757-7.00010-4

Figures and Tables

Figure 1. NF1 is differentially mutated in metastatic vs primary HER2+ BC and its loss leads to differential sensitivity to anti-HER2 agents

a. Comparison of mutation frequency in unmatched metastatic *vs* primary tumours in the or *ERBB2*-amplified cohort of BC, from TCGA and MSK-IMPACT. Plot depicts odds ratio (OR) *vs* -log p value of mutation frequency **b.** Lollipop plots depicting frequency of point mutations in metastatic *vs* primary breast tumours in *ERBB2*-amplified cohorts. **c.** Structural representation of the neurofibromin dimer and its domains, color-coded as in 1c: CSRD (cysteine- and serine-rich domain), TBD (tubulin-binding domain), GRD (GAP-related domain), Sec14/PH (Sec14 homologous domain and pleckstrin homologous domain), LRD (leucin-rich domain), and CTD (C-terminal domain). **d.** IC50 values in short-term (3 days) BrdU incorporation assays of BT-474^{WT} and BT-474^{KO} cells exposed to the indicated agents. **e** Co-culture of H2B-GFP or H2B-mCherry-expressing BT-474^{WT} and BT-474^{KO} cells at baseline; stacked bar expressing population percentages over time upon treatment with T-DM1 as indicated.

Figure 2 NF1 loss leads to increased G2/M arrest and apoptosis upon T-DM1 treatment

a. b. Propidium-iodide (PI) cell cycle analysis after 36h of T-DM1 at the indicated doses; **** $p < 0.0001$, $\chi 2$ test; error bars are SD. Data was reproducible with other cell lines (not shown). **c.** Round-up figures on BT-474^{KO} and BT-474^{WT} cells, indicative of ongoing terminal mitosis, can be observed in phase contrast microscopy (EVOS® FL Cell Imaging System) after 24h of T-DM1 treatment. **d.** quantification of **c.** $p = 0.0004$, Fisher's exact test; error bars are SD. **e.** Whole cell lysates of HCC1954^{WT} and HCC1954^{KO} blotted for cleaved PARP and Bcl-2 at 48h after T-DM1 treatment. **f.** G1 (red), S (green) G2/M (yellow), and DRAQ7TM (white) - a live- cell impermeable, far-red emitting DNA dye that marks for cell death - are represented at 0h and 90h. **g.** Cell fate analysis of 200 cells/condition during 90h of T-DM1 exposure, showing a reduction in proliferating cells, longer G2/M arrest and higher G1 prevalence across time in BT-474^{KO} cells compared to BT-474^{WT}. **h.** cell viability curves through time of BT-474^{WT} and BT-474^{KO} cells treated with T-DM1 **i.** Ridgeline and box plots showing the distribution and quantification of cell fraction according to time spent in G2/M phase of BT-474^{WT} and BT-474^{KO} cells upon T-DM1 treatment. Wilcoxon test shows significant differences (p value<0.001) among NF1 KO and WT for each treatment dose. **j.** Experimental design **k.** Bioluminescent images and **l.** growth of HCC1954 WT and HCC1954 KO xenograft mammary tumors treated biweekly with vehicle or T-DM1 (4 mg/kg); n = 10 mice per group, means of total flux (photons/s) with SD are plotted. **m.** hematoxylin-eosin (HE) and Cleaved Caspase 3 staining of tumor

masses isolated 24 hours after T-DM1 treatment **n.** quantification of data in m. One-way ANOVA with Tukey post-hoc analysis. *p<0.05

Figure 3. NF1 loss-associated hypersensitivity to T-DM1 is due to the DM1 payload and is RAS-independent

a. 8-days growth curves on BT-474 WT and BT-474 NF1 KO cells treated with DM1, T-DM1 and T-DXd. Rituximab, a human IgG1 monoclonal antibody, and DMSO were used as control. To draw the ribbon in log10 scale, non-positive lower boundaries (time-point 8, KO, DM1 and TDM1) were substituted by the value 5000. 3-way ANOVA tests for time series (see methods) **b.** Colony formation assay for HCC1954 and BT-474 cell lines treated with T-DM1 **c.** DM1 **d.** Trastuzumab and **e.** T-DXd **f.** Active Ras pull-down in BT-474 WT and BT-474 G12V cells **g.** 8-days growth curves with DM1, T-DM1 on BT-474^{WT} and BT-474^{G12V} cells. To draw the ribbon in log10 scale, non-positive lower boundaries (time 8, RAS OE, DM1 and TDM1) were substituted by the value 5000.

Figure 4 NF1loss leads to mitotic aberrations and aneuploidy

a-c RNAseq in BT-474^{KO} and BT-474^{WT} cells treated with T-DM1 at 1 µg/ml for 36 hours a. Principal Component Analysis of 3 independent biological replicates per condition. **b**. Comparison of transcriptional changes, expressed as log2 fold change of treated vs untreated, per genotype. Highlighted genes are significantly more downregulated in BT-474^{KO} vs BT-474^{WT} in response to T0-DM1 **c.** gene ontology analysis of highlighted genes in figure 4b. **d-f** live cell imaging of BT-474^{KO} and BT-474^{WT} cells stably expressing H2B-GFP/H2B-mCherry and monitored over 100 minutes, with acquisitions every 4 minutes. Cells were incubated with cell-permeable, fluorescent Sir-tubulin to monitor spindle formation. **d**. representative frames. Arrows point to the indicated aberrations **e**. quantification of mitosis length, indicated as time from Nuclear Envelope BreakDown (NEBD) to anaphase end. **f**. frames representative of an event of multipolar division in BT-474^{KO} cells. g-h mitotic plate measurement in BT-474^{KO} and BT-474^{WT} **g**. representative images h quantification of plate width i-j measurement of centrosome numbers in synchronized HCC1954^{WT} and HCC1954^{KO} cells. **i** representative fields from cells synchronized by RO3306. Cells are stained with anti-alpha tubulin and the centrosome marker Cep63. **j** quantification of data in i and of separate experiments with double thymidine block synchronization. **k-l** quantification of chromosome missegregation in BT-474^{WT} and two independently derived KO BT474 clones. The centromere marker CREST is used to identify centromeres; **l** quantification of data from experiment in k; **m-n** quantification of polyploidy by propidium iodide and BrdU staining by flow cytometry in BT-474^{KO} and BT-474^{WT} cells; **m** representative FACS plots; **n** quantification of data in m; all statistical tests ine, h, j, l, n by Wilcoxon test; **p<0.01, ***p<0.001, ****p<0.0001; lines represent mean ± SD; **o-p** aneuploidy score in patients with breast cancer in the AACR Genie cohort; **o** flow diagram of patient selection strategy. NF1-mutated patients were selected for the presence of variants pathogenic according to alpha missense. **p** quantification of the ASCETS-computed aneuploidy score in NF1-mutated vs -nonmutated patients. *p<0.05 by Wilcoxon test

Figure 5. NF1 is a microtubule-associated protein (MAP)

a. Immunofluorescence on Rho3306-synchronized HCC1954 cell lines with anti-NF1 and anti-tubulin antibodies. **b**. co-sedimentation of NF1 with Taxol-stabilized microtubules. NuMa, a known microtubules binding protein, was used as positive control. S=supernatant, P=pellet. **c**. Turbidity assay. Tubulin (20 mM) was incubated alone or in combination with drugs or NF1 as indicated at 37°C. Polymerization was followed by continuous (1 reading per minute) reading of absorbance at 340nm over a 60 min period, in a temperature-stabilized spectrophotometer. **d**. Taxol-stabilized rhodamine-labeled microtubules were incubated in the absence or presence of NF1 at room temperature for 10 min before acquiring fluorescence microscopy images. **e**. Representative kymographs of microtubules grown in vitro with or without NF1 from GMPCPP-stabilized seeds and followed by TIRF microscopy. NF1 increases the fraction of microtubules initiating elongation. **f-h** quantification of microtubular dynamics parameters **f**: percentage of elongating microtubules, calculated as the number of GMPCPP seeds elongating divided by the total number of seeds present in the acquired ROI. **g,** growth speed. **h** rescue frequency, calculated by dividing the number of rescues observed by the total shrinkage length. Data are means ± SEM from two

independent experiments. Kruskal-Wallis test with Dunn post-hoc test was used to assess significance. *** $p<0.01$

Figure 6. DM1 leads to intratubular damage that is repaired more efficiently in the presence of NF1
a-c CETSA for DM1 in BT-474^{WT} and BT-474^{KO} cells. **a** experimental design. Cells are harvested and incubated in suspension with DM1 for 2h and then exposed to increasing temperatures as indicated **b** western blot for β-tubulin of cell extracts from BT-474^{WT} and BT-474^{KO} cells**. c.** Quantification of band intensities from CETSA western blots (n = 3 independent experiments), normalised on baseline signal at 57°C. Ribbons indicate SD. We used 2-way ANOVA separately on WT and KO to test for significance of temperature and drug. We observed that temperature was significant both in the WT and in the KO case (pvalue=2.05×10^{-12} and 1.79×10^{-9}, respectively). However, the addition of DM1 was significant only in the KO case (pvalue=4.62×10^{-3}, 0.78 in the WT case). **d.** Representative kymographs of microtubules grown in vitro with or without NF1 at indicated concentration and 1µM DM1 from GMPCPP-stabilized seeds and followed by TIRF microscopy **e.** NF1 increases the fraction of microtubules initiating elongation in the presence of 1µM DM1. The percentage for each condition was calculated as the number of GMPCPP seeds elongating divided by the total number of seeds present in the acquired ROI. **f.** Quantification of growth rate of microtubules grown with 1µM DM1 and with 100nM or 300nM NF1. **g.** Quantification of depolymerization rate of microtubules grown with or without 100nM NF1 and with or without 1µM DM1. Data are means ± SEM. Kruskal-wallis test with Dunn post-hoc test was used to assess significance. **h.** Single frames of time-lapse videos of taxol-stabilized rhodamine-labeled microtubules incubated with 1µM DM1 **i.** Taxol-stabilized rhodamine-labeled microtubules were first incubated without Taxol and tubulin for 1.5 min and subsequently with 5 mM HiLyte Fluor-488-labeled tubulin with 100nM NF1. After 10 min, the residual free green tubulin was washed out with the wash buffer supplemented with 25% glycerol to prevent microtubule depolymerization, in order to better visualize incorporation of green tubulin. Kymograph showing green tubulin incorporation sites into Rhodamine-labelled microtubule lattices (magenta). Arrows indicate complete repair. **j.** reconstruction of microtubule tip trajectories after monitoring of microtubule elongation in BT-474^{WT} and BT-474^{KO} cells transiently transfected with an EB3-GFP-expressing vector and monitored by live cell imaging for 1 minute with acquisitions every 4 seconds. Microtubule tip fates were reconstructed by the TrackMate ImageJ plugin. **k** quantification of tip mean speed. At least 1000 events from at least 3 cells were calculated per condition. 2-way ANOVA with Tukey's HSD. **** $p < 0.001$. **l-m** immunofluorescence for acK40 alpha tubulin in HCC1954^{WT} and HCC1954^{KO} . **m** quantification of mean intensity normalized by area occupied by cell cytoplasm. 4 fields of view per condition

Supplementary files:

Supplementary figures 1-4
Supplementary movies 1-13
Supplementary tables 1-3

Supplementary figure legends:

Supplementary figure 1
a. Comparison of mutation frequency in unmatched metastatic *vs* primary tumours in unsorted BC, from TCGA and AACR-GENIE. Plot depicts odds ratio (OR) *vs* -log p value of mutation frequency; **b.** Lollipop plots depicting frequency of point mutations in metastatic *vs* primary breast tumours in unsorted BC cohorts. **c**. assessment of NF1 protein loss in multiple clones of CRISPR-Cas9-engineered BT-474, SK-BR3 and HCC1954 cells, using multiple NF1 antibodies. **d** representative IGV visualizations of the NF1 genomic region surrounding the guide RNA target site, in WT and Cas9-engineered clones **e**. representative FACS plots of co-cultures of H2B-GFP- or H2B-mCherry-expressing BT-474^{WT} and BT-474^{KO} cells at baseline

Supplementary figure 2

a beta-galactosidase activity in BT-474^{WT} and BT-474^{KO} cells treated with vehicle (DMSO), T-DM1 (1 µg/ml) and Doxorubicin (200 nM) for 5 days. On the right, quantification by integrated density; **b** phase transitions in FUCCI(Ca)-expressing cells, relative to the experiment described in figure 2G.

Supplementary figure 3

a. assessment of HER2 expression in BT-474^{WT} and BT-474^{KO} cells by flow cytometry **b**. T-DM1 internalization assay. BT-474^{WT} and BT-474^{KO} were incubated with vehicle or T-DM1 (1 µg/ml) for 24hr, with or without chloroquine (5 µM) to block lysosomal HER2 degradation. Cells were then fixed and stained with an anti-human HER2 antibody, and the total fluorescence per cell measured and normalized by cell area. On the right, quantification. Wilcoxon test was not significant in the WT vs KO comparison in any condition; **c**. short-term (3 days) BrdU-based dose response curves of multiple microtubule-targeting agents. Known tubulin binding sites are color-coded on the tubulin dimer structure. **d** active RAS pulldown of wild-type, NF1 Ko or RAS G12V-expressing SK-BR3 cells

Supplementary figure 4

a. validation of the NF1-A 376G3 antibody for immunofluorescence. HCC1954^{WT} and HCC1954^{KO} cells were incubated with the indicated antibodies and identical microscope settings were applied for acquisition **b.** NF1 purifies as a single peak by size-exclusion chromatography. **c.** Purified recombinant NF1 is highly pure by SDS-PAGE. **d.** Western blot analysis of the purified recombinant NF1 shows the efficiency of the 6XHIS-tag cut. **e.** Mass photometry histogram; peaks are fit by Gaussian curves. The peak corresponds to NF1 dimers **f.** NF1 accelerates the hydrolysis of GTP by RAS. Hydrolysis was measured by GTPase-Glo kit to detect the amount of GTP remaining in the reaction after incubation. **g.** Calculation of the critical tubulin concentration for polymerization. Each point represents a reaction in which unpolymerized tubulin at the indicated concentrations was allowed to polymerize and OD recorded. We interpolated OD levels and 0 in both conditions. The intersection with X-axis is the Critical concentration (CC) (see arrows).

Supplementary movie legends

Supplementary movie 1: live cell imaging of BT-474^{WT} cells stably expressing H2B-GFP and monitored over 100 minutes, with acquisitions every 4 minutes. Cells were incubated with cell-permeable, fluorescent SiR-tubulin to monitor spindle formation.

Supplementary movie 2: live cell imaging of BT-474^{KO} cells stably expressing H2B-mCherry and monitored over 100 minutes, with acquisitions every 4 minutes. Cells were incubated with cell-permeable, fluorescent SiR-tubulin to monitor spindle formation. A longer mitosis with transient multipolar state can be appreciated.

Supplementary movie 3: live cell imaging of BT-474^{KO} cells stably expressing H2B-mCherry and monitored over 100 minutes, with acquisitions every 4 minutes. Cells were incubated with cell-permeable, fluorescent SiR-tubulin to monitor spindle formation. A multipolar cell division can be appreciated.

Supplementary movie 4: TIRF microscopy monitoring of microtubule dynamics, followed over 20 min with an acquisition every 10 seconds. GMPCPP seeds are shown in magenta, free tubulin in cyan. No NF1, No DM1 added.

Supplementary movie 5: TIRF microscopy monitoring of microtubule dynamics, followed over 20 min with an acquisition every 10 seconds. GMPCPP seeds are shown in magenta, free tubulin in cyan. NF1 added at 100 nM.

Supplementary movie 6: TIRF microscopy monitoring of microtubule dynamics, followed over 20 min with an acquisition every 10 seconds. GMPCPP seeds are shown in magenta, free tubulin in cyan. NF1 added at 300 nM.

Supplementary movie 7: TIRF microscopy monitoring of microtubule dynamics, followed over 20 min with an acquisition every 10 seconds. GMPCPP seeds are shown in magenta, free tubulin in cyan. No NF1, DM1 1 µM.

Supplementary movie 8: TIRF microscopy monitoring of microtubule dynamics, followed over 20 min with an acquisition every 10 seconds. GMPCPP seeds are shown in magenta, free tubulin in cyan. NF1 added at 100 nM, DM1 1 µM.

Supplementary movie 9: TIRF microscopy monitoring of microtubule dynamics, followed over 20 min with an acquisition every 10 seconds. GMPCPP seeds are shown in magenta, free tubulin in cyan. NF1 added at 300 nM, DM1 1 µM.

Supplementary movie 10: monitoring of microtubule elongation in BT-474^{WT} cells transiently transfected with an EB3-GFP-expressing vector and monitored by live cell imaging for 1 minute with acquisitions every 4 seconds.

Supplementary movie 11: monitoring of microtubule elongation in BT-474^{KO} cells transiently transfected with an EB3-GFP-expressing vector and monitored by live cell imaging for 1 minute with acquisitions every 4 seconds.

Supplementary movie 12: monitoring of microtubule elongation in BT-474^{WT} cells transiently transfected with an EB3-GFP-expressing vector and monitored by live cell imaging for 1 minute with acquisitions every 4 seconds. DM1 added at 0.5 nM.

Supplementary movie 11: monitoring of microtubule elongation in BT-474^{KO} cells transiently transfected with an EB3-GFP-expressing vector and monitored by live cell imaging for 1 minute with acquisitions every 4 seconds. DM1 added at 0.5 nM.

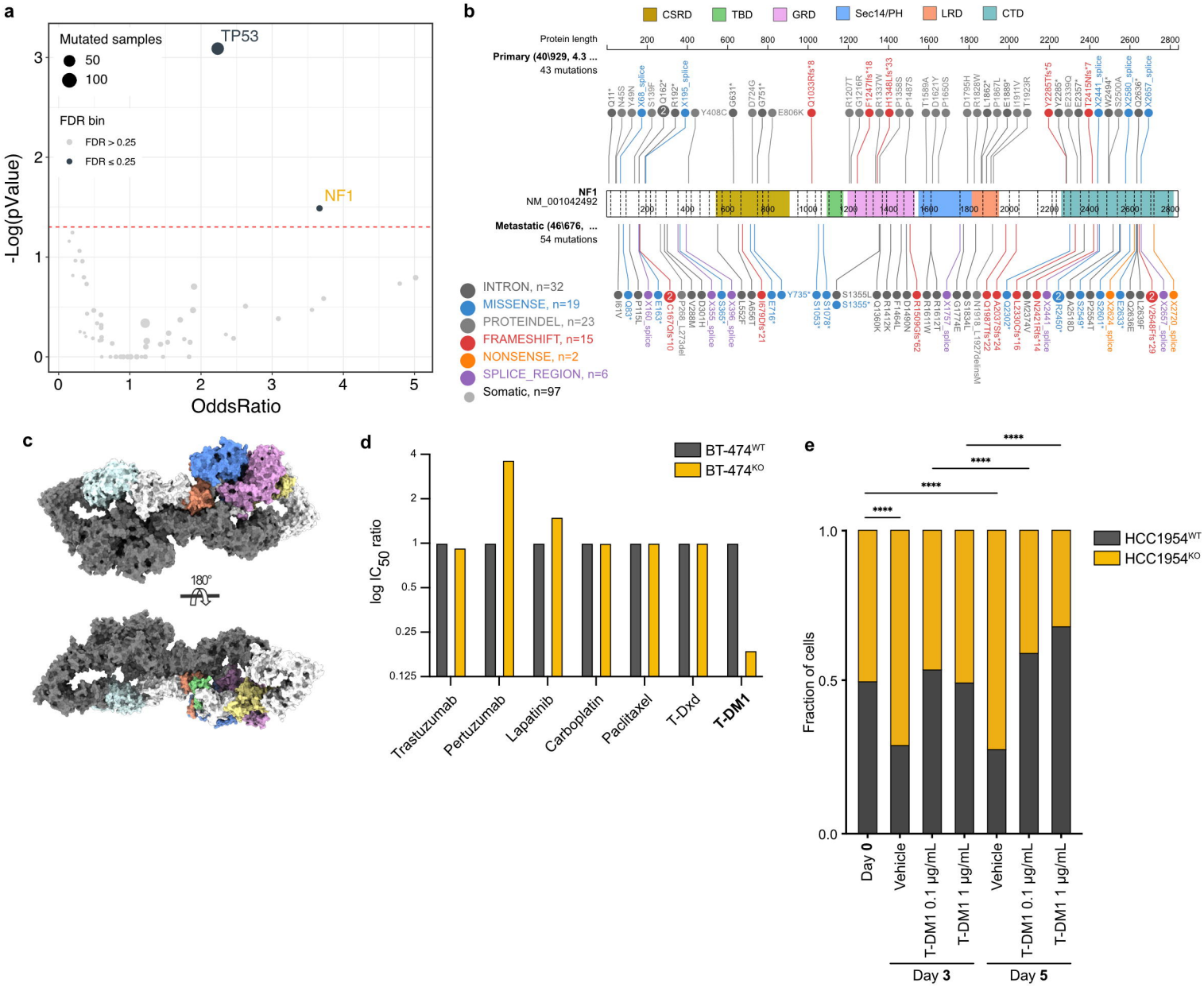
a
Mutated samples
50
100
FDR bin
FDR > 0.25
FDR ≤ 0.25
TP53
NF1
-Log(pValue)
OddsRatio
b
CSRD
TBD
GRD
Sec14/PH
LRD
CTD
Protein length
Primary (40\929, 4.3 ...
43 mutations
NF1
NM_001042492
Metastatic (46\676, ...
54 mutations
INTRON, n=32
MISSENSE, n=19
PROTEINDEL, n=23
FRAMESHIFT, n=15
NONSENSE, n=2
SPLICE_REGION, n=6
Somatic, n=97
c
180°
d
BT-474WT
BT-474KO
log IC50 ratio
Trastuzumab
Pertuzumab
Lapatinib
Carboplatin
Paclitaxel
T-Dxd
T-DM1
e
HCC1954WT
HCC1954KO
Fraction of cells
Day 0
Vehicle
T-DM1 0.1 µg/mL
T-DM1 1 µg/mL
Day 3
Day 5

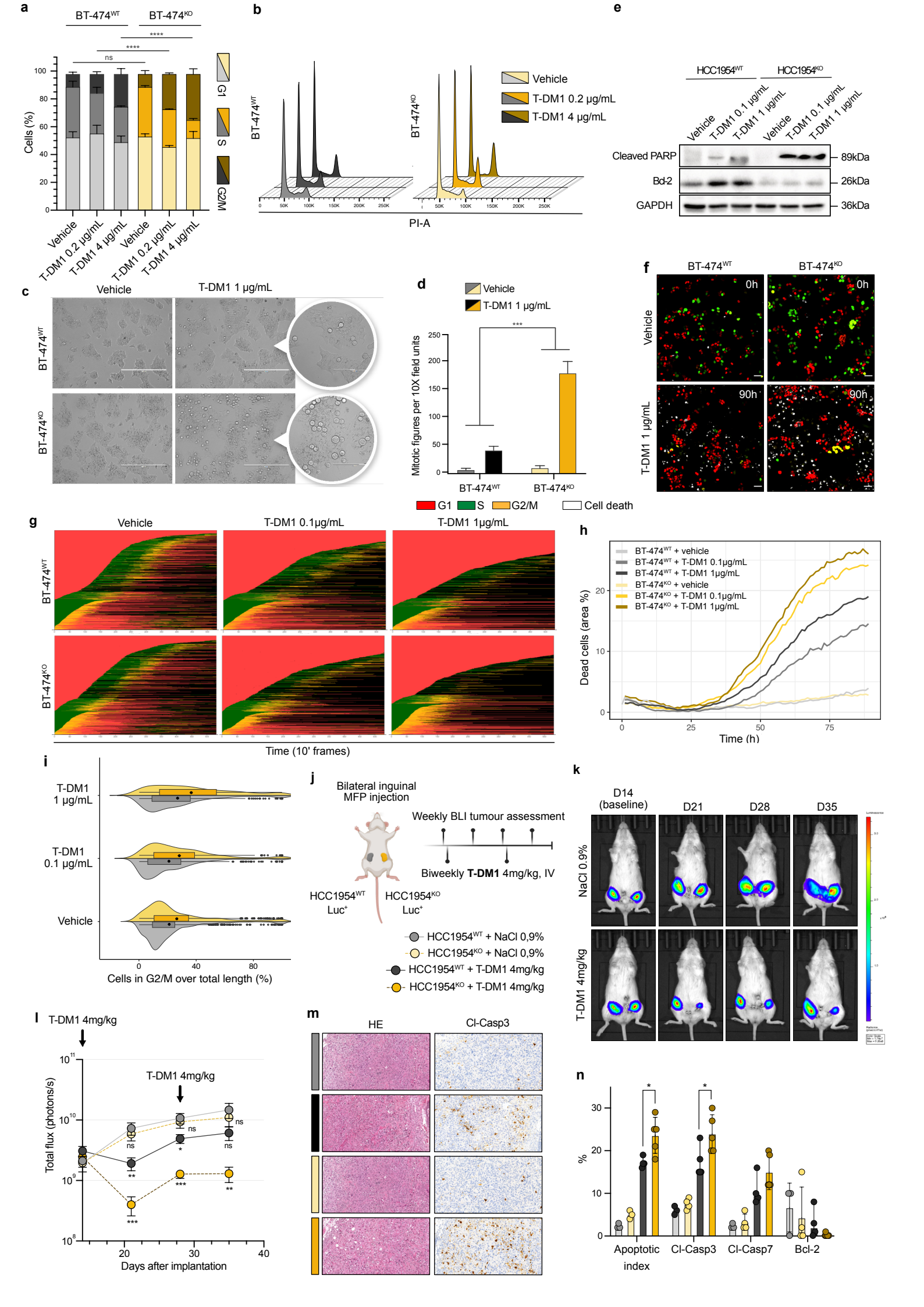
a
BT-474WT
BT-474KO
Cells (%)
G1
S
G2/M
Vehicle
T-DM1 0.2 µg/mL
T-DM1 4 µg/mL
b
BT-474WT
BT-474KO
Vehicle
T-DM1 0.2 µg/mL
T-DM1 4 µg/mL
PI-A
e
HCC1954WT
HCC1954KO
Vehicle
T-DM1 0.1 µg/mL
T-DM1 1 µg/mL
Cleaved PARP
Bcl-2
GAPDH
89kDa
26kDa
36kDa
c
Vehicle
T-DM1 1 µg/mL
d
Mitotic figures per 10X field units
f
0h
90h
g
T-DM1 0.1µg/mL
T-DM1 1µg/mL
Time (10' frames)
h
BT-474WT + vehicle
BT-474WT + T-DM1 0.1µg/mL
BT-474WT + T-DM1 1µg/mL
BT-474KO + vehicle
BT-474KO + T-DM1 0.1µg/mL
BT-474KO + T-DM1 1µg/mL
Dead cells (area %)
Time (h)
i
T-DM1 1 µg/mL
T-DM1 0.1 µg/mL
Cells in G2/M over total length (%)
j
Bilateral inguinal MFP injection
Weekly BLI tumour assessment
Biweekly T-DM1 4mg/kg, IV
HCC1954WT Luc+
HCC1954KO Luc+
HCC1954WT + NaCl 0,9%
HCC1954KO + NaCl 0,9%
HCC1954WT + T-DM1 4mg/kg
HCC1954KO + T-DM1 4mg/kg
k
D14 (baseline)
D21
D28
D35
NaCl 0,9%
T-DM1 4mg/kg
l
T-DM1 4mg/kg
Total flux (photons/s)
Days after implantation
m
HE
Cl-Casp3
n
%
Apoptotic index
Cl-Casp3
Cl-Casp7
Bcl-2

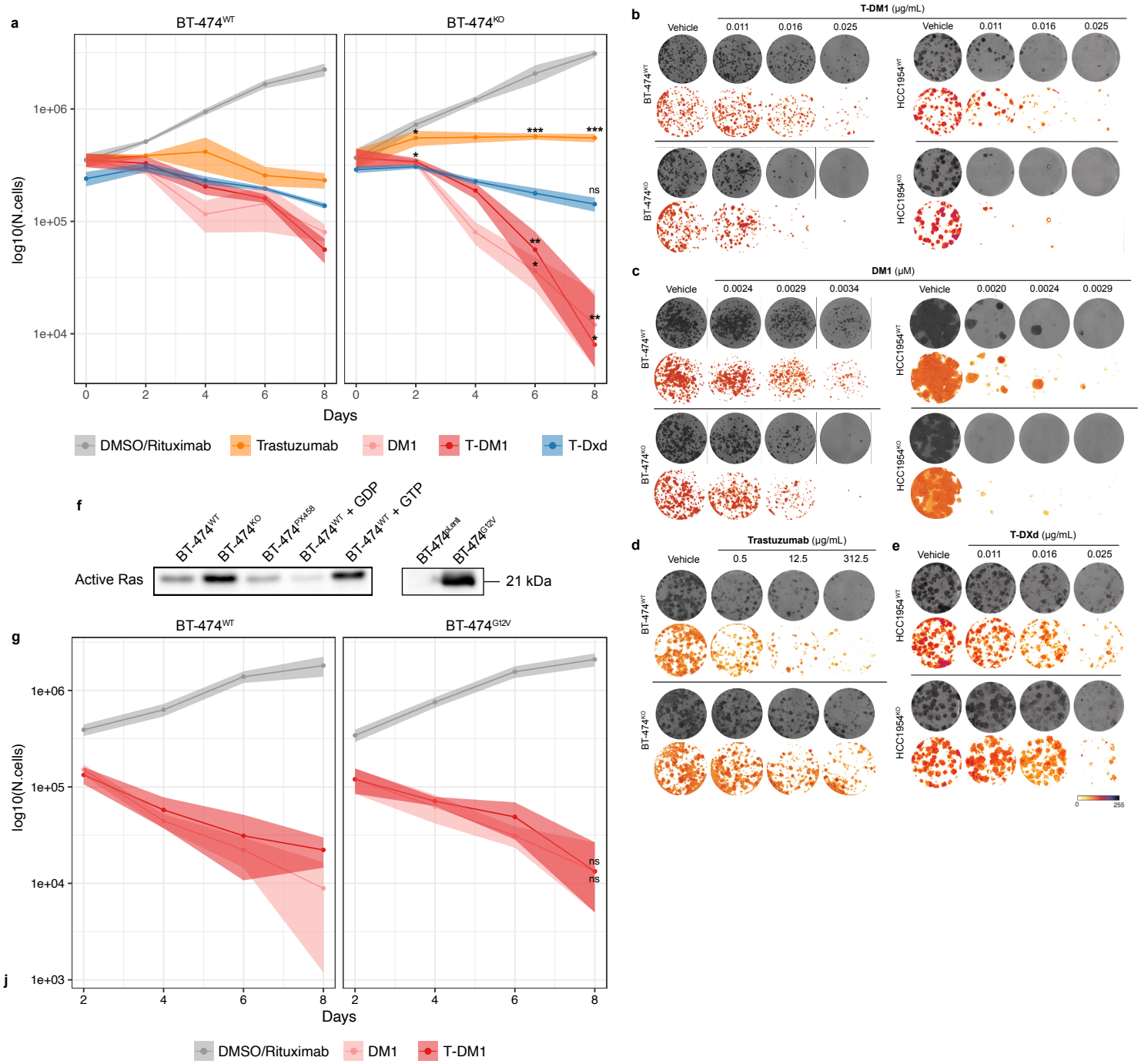
a
BT-474WT
BT-474KO
log10(N.cells)
1e+06
1e+05
1e+04
Days
DMSO/Rituximab
Trastuzumab
DM1
T-DM1
T-Dxd
b
T-DM1 (µg/mL)
Vehicle
0.011
0.016
0.025
BT-474WT
BT-474KO
HCC1954WT
HCC1954KO
c
DM1 (µM)
0.0024
0.0029
0.0034
0.0020
d
Trastuzumab (µg/mL)
0.5
12.5
312.5
e
T-DXd (µg/mL)
f
BT-474WT
BT-474KO
BT-474PX458
BT-474WT + GDP
BT-474WT + GTP
BT-474pLenti
BT-474G12V
Active Ras
21 kDa
g
BT-474WT
BT-474G12V
1e+03
j
DMSO/Rituximab
DM1
T-DM1

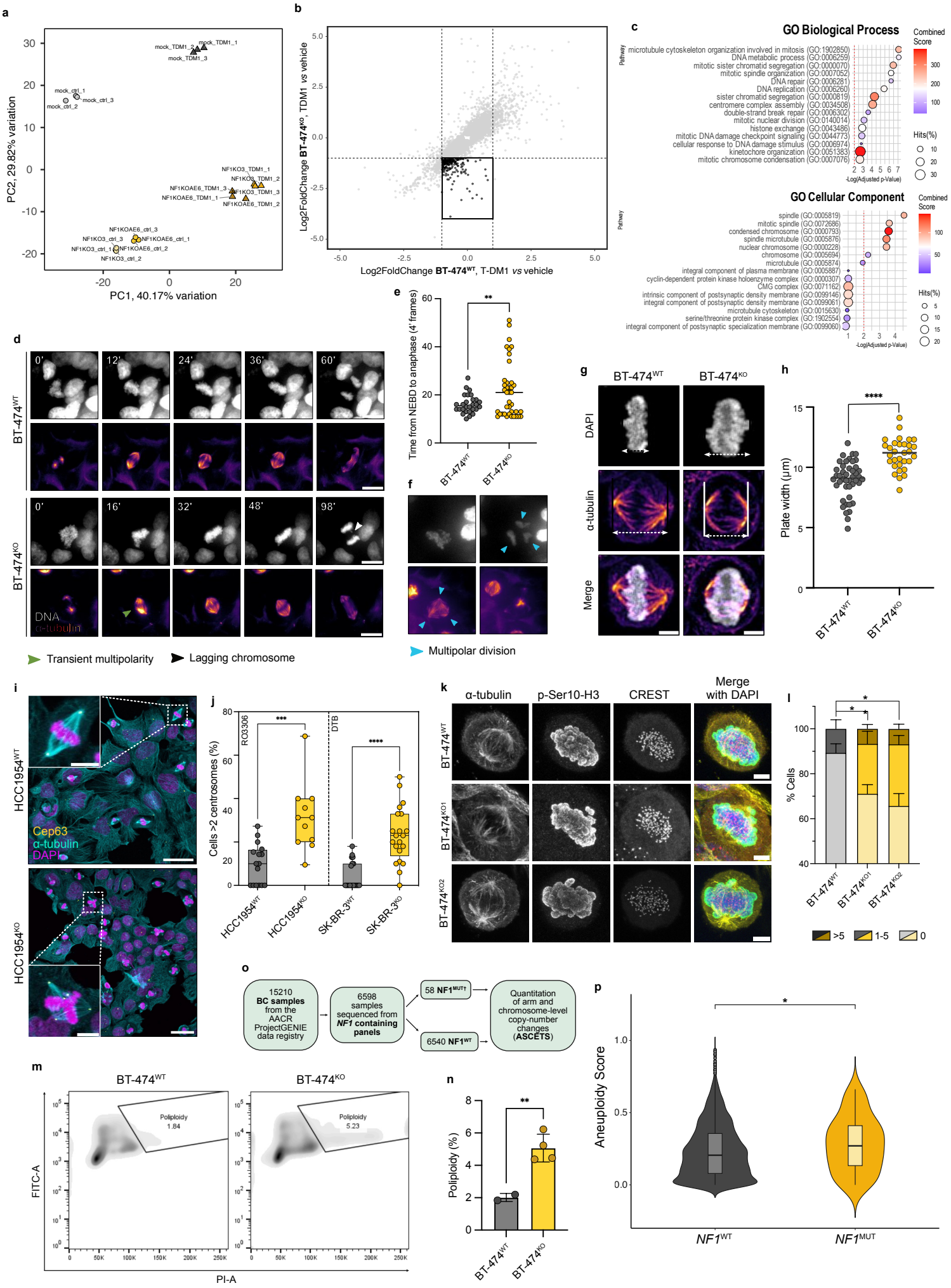
a
PC2, 29.82% variation
PC1, 40.17% variation
mock_TDM1_1
mock_TDM1_2
mock_TDM1_3
mock_ctrl_1
mock_ctrl_2
mock_ctrl_3
NF1KO3_TDM1_1
NF1KO3_TDM1_2
NF1KO3_TDM1_3
NF1KOAE6_TDM1_1
NF1KOAE6_TDM1_2
NF1KOAE6_TDM1_3
NF1KOAE6_ctrl_1
NF1KOAE6_ctrl_2
NF1KOAE6_ctrl_3
NF1KO3_ctrl_1
NF1KO3_ctrl_2
NF1KO3_ctrl_3
b
Log2FoldChange BT-474KO, TDM1 vs vehicle
Log2FoldChange BT-474WT, T-DM1 vs vehicle
c
GO Biological Process
microtubule cytoskeleton organization involved in mitosis (GO:1902850)
DNA metabolic process (GO:0006259)
mitotic sister chromatid segregation (GO:0000070)
mitotic spindle organization (GO:0007052)
DNA repair (GO:0006281)
DNA replication (GO:0006260)
sister chromatid segregation (GO:0000819)
centromere complex assembly (GO:0034508)
double-strand break repair (GO:0006302)
mitotic nuclear division (GO:0140014)
histone exchange (GO:0043486)
mitotic DNA damage checkpoint signaling (GO:0044773)
cellular response to DNA damage stimulus (GO:0006974)
kinetochore organization (GO:0051383)
mitotic chromosome condensation (GO:0007076)
Combined Score
Hits(%)
-Log(Adjusted p-Value)
GO Cellular Component
spindle (GO:0005819)
mitotic spindle (GO:0072686)
condensed chromosome (GO:0000793)
spindle microtubule (GO:0005876)
nuclear chromosome (GO:0000228)
chromosome (GO:0005694)
microtubule (GO:0005874)
integral component of plasma membrane (GO:0005887)
cyclin-dependent protein kinase holoenzyme complex (GO:0000307)
CMG complex (GO:0071162)
intrinsic component of postsynaptic density membrane (GO:0099146)
integral component of postsynaptic density membrane (GO:0099061)
microtubule cytoskeleton (GO:0015630)
serine/threonine protein kinase complex (GO:1902554)
integral component of postsynaptic specialization membrane (GO:0099060)
d
BT-474WT
BT-474KO
0'
12'
24'
36'
60'
16'
32'
48'
98'
DNA
α-tubulin
Transient multipolarity
Lagging chromosome
e
Time from NEBD to anaphase (4' frames)
f
Multipolar division
g
BT-474WT
BT-474KO
DAPI
α-tubulin
Merge
h
Plate width (µm)
i
HCC1954WT
HCC1954KO
Cep63
α-tubulin
DAPI
j
Cells >2 centrosomes (%)
RO3306
DTB
HCC1954WT
HCC1954KO
SK-BR-3WT
SK-BR-3KO
k
α-tubulin
p-Ser10-H3
CREST
Merge with DAPI
BT-474WT
BT-474KO1
BT-474KO2
l
% Cells
>5
1-5
0
o
15210 BC samples from the AACR ProjectGENIE data registry
6598 samples sequenced from NF1 containing panels
58 NF1MUT†
6540 NF1WT
Quantitation of arm and chromosome-level copy-number changes (ASCETS)
m
BT-474WT
BT-474KO
Poliploidy 1.84
Poliploidy 5.23
FITC-A
PI-A
n
Poliploidy (%)
p
Aneuploidy Score
NF1WT
NF1MUT

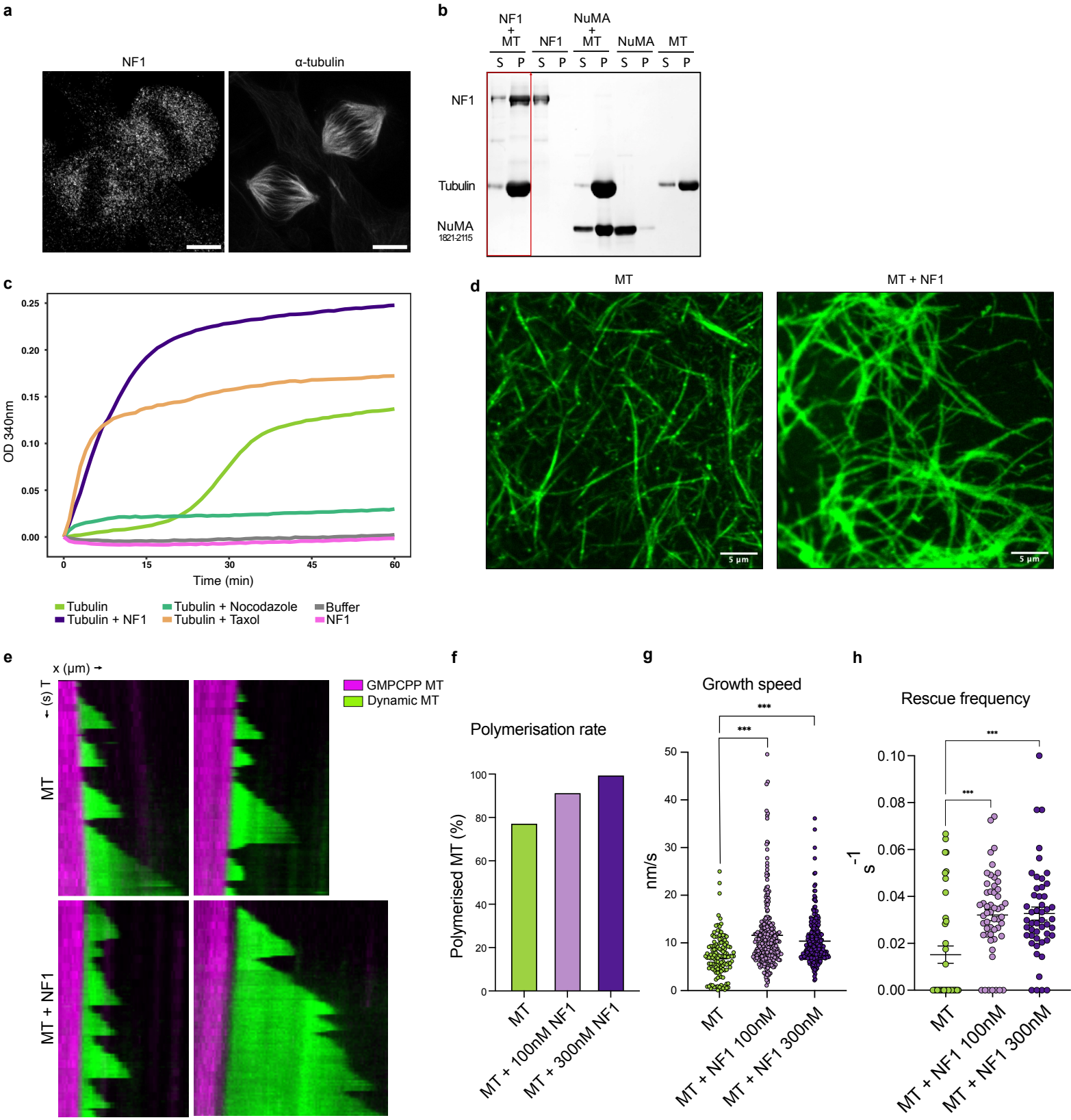
a
NF1
α-tubulin
b
NF1 + MT
NF1
NuMA + MT
NuMA
MT
S P S P S P S P S P
NF1
Tubulin
NuMA 1821-2115
c
OD 340nm
Time (min)
Tubulin
Tubulin + NF1
Tubulin + Nocodazole
Tubulin + Taxol
Buffer
NF1
d
MT
MT + NF1
5 µm
e
x (µm)
t (s)
MT
MT + NF1
GMPCPP MT
Dynamic MT
f
Polymerisation rate
Polymerised MT (%)
MT
MT + 100nM NF1
MT + 300nM NF1
g
Growth speed
nm/s
MT
MT + NF1 100nM
MT + NF1 300nM
h
Rescue frequency
s-1
MT
MT + NF1 100nM
MT + NF1 300nM

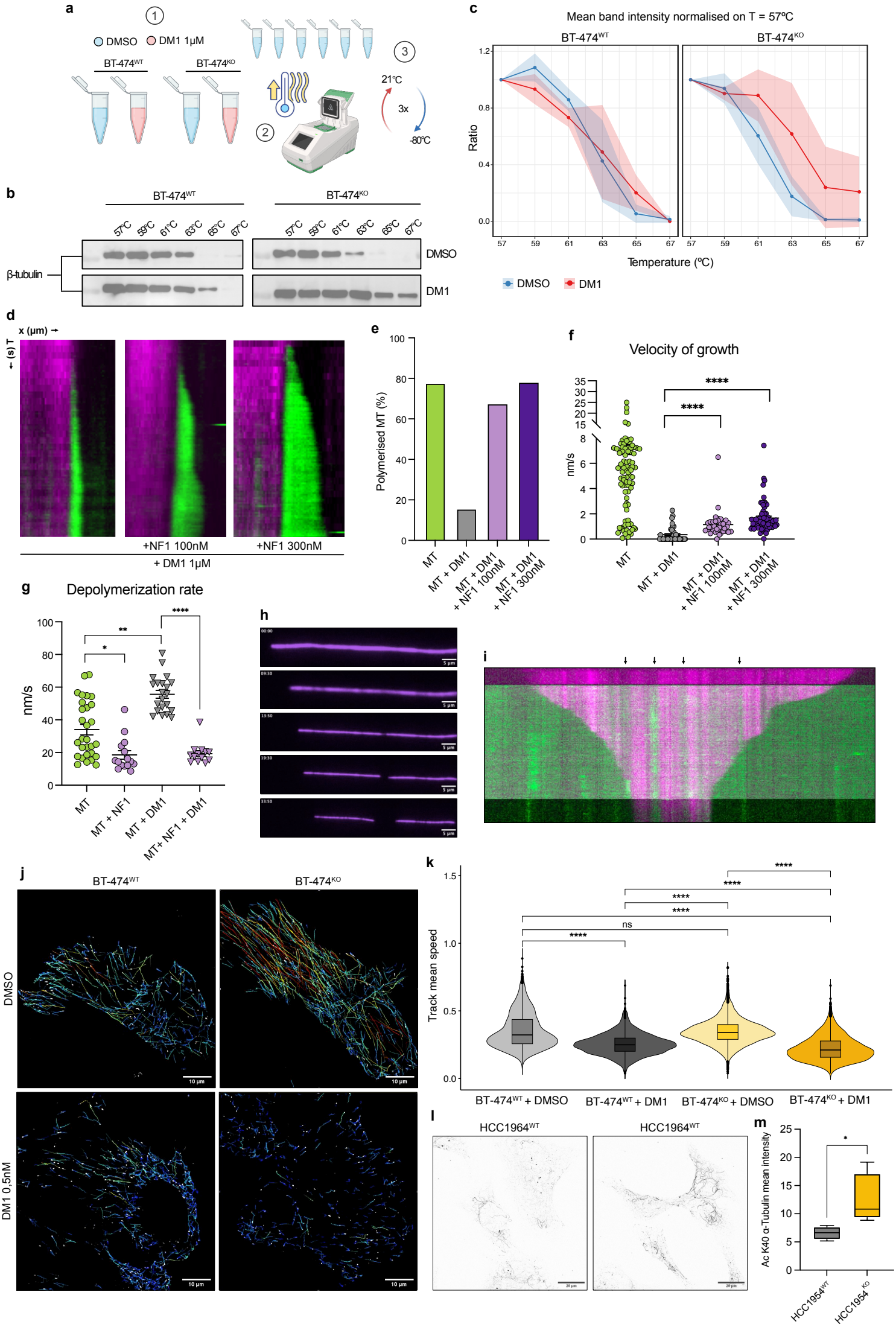
a
1
DMSO
DM1 1µM
BT-474WT
BT-474KO
2
3
21°C
3x
-80°C
b
BT-474WT
BT-474KO
57°C
59°C
61°C
63°C
65°C
67°C
β-tubulin
DMSO
DM1
c
Mean band intensity normalised on T = 57°C
BT-474WT
BT-474KO
Ratio
Temperature (°C)
DMSO
DM1
d
x (µm) →
← (s) T
+NF1 100nM
+NF1 300nM
+ DM1 1µM
e
Polymerised MT (%)
MT
MT + DM1
MT + DM1 + NF1 100nM
MT + DM1 + NF1 300nM
f
Velocity of growth
nm/s
****
****
MT
MT + DM1
MT + DM1 + NF1 100nM
MT + DM1 + NF1 300nM
g
Depolymerization rate
nm/s
**
*
****
MT
MT + NF1
MT + DM1
MT+ NF1 + DM1
h
i
j
BT-474WT
BT-474KO
DMSO
DM1 0,5nM
10 µm
k
Track mean speed
****
****
****
****
ns
****
BT-474WT + DMSO
BT-474WT + DM1
BT-474KO + DMSO
BT-474KO + DM1
l
HCC1964WT
HCC1964WT
m
Ac K40 α-Tubulin mean intensity
*
HCC1954WT
HCC1954KO